1 Fluid geochemistry of the Cerro Galán geothermal system (Southern Puna, Argentina):

2 Implications for the geothermal potential of one of the youngest giant calderas in the

3 Andes

4

5 Chiodi A.[1,*], Báez W.[1], Tassi F.[2,3], Bustos E. [1], Filipovich R. [1], Murray J. [1,4], Rizzo, A.L.[5,6], Vaselli,

6 O.[2,3,], Giordano G.[7], Viramonte J.G.[1]

7

8 [1] Instituto de Bio y Geociencias del NOA (IBIGEO, UNSa-CONICET), Av. 9 de Julio 14, A4405BBA

9 Salta, Argentina. e-mail address: a.chiodi@conicet.gov.ar

10 [2] Department of Earth Sciences, University of Florence, Via La Pira 4, 50121 Florence, Italy

11 [3] CNR-IGG Institute of Geosciences and Earth Resources, Via La Pira 4, 50121 Florence, Italy

12 [4] Institut Terre et Environnement de Strasbourg (ITES), Université de Strasbourg, CNRS, UMR 7063,

13 5 rue René Descartes, 67084, Strasbourg, France

14 [5] Department of Earth and Environmental Sciences, University of Milan-Bicocca, Piazza dell' Scienza,

15 20126, Milan, Italy

16 [6] Istituto Nazionale di Geofisica e Vulcanologia, Sezione di Milano, Via Alfonso Corti 12, 20133

17 Milan Italy

18 [7] Università degli Studi di Roma Tre, Dipartimento di Scienze, Largo S. L. Murialdo 1, 00146 Rome,

19 Italy

20

21 ## Abstract

22 The exploration of novel geothermal systems, particularly those promising for electrical power

23 generation, plays a fundamental role in incorporating new renewable sources into the energy matrix.

24 Geothermal systems associated with volcanic calderas are considered ideal targets for exploration.

25 This study focuses on the geochemical features of fluids from the Cerro Galán hydrothermal system,

26 which is hosted within a major resurgent caldera with more than 3.5 Myr of magmatic evolution

27 situated on the Southern Puna (Central Volcanic Zone of the Andes, NW Argentina). The main aim is

28 constructing the first geochemical conceptual model and provide information on the geothermal

29 potential of this interesting resource. The main hydrothermal reservoir consists of a Na-Cl aquifer with

30 estimated temperatures up to 187 °C at depth. This reservoir is likely hosted within the fractured pre-

31 caldera basement rocks, mainly including Miocene-Pliocene volcanic rocks and Proterozoic-Cambrian

32 igneous and metamorphic rocks. The confinement of the deep reservoir is attributed to the deposits of

33 the Toconquis Group and Cueva Negra Ignimbrite, along with the basal section of the Cerro Galán

Ignimbrite, which exhibit low permeability due to hydrothermal alteration. The presence of a phreatic explosion crater near one of the hot spring-rich areas is likely indicating past over-pressurization of the hydrothermal aquifer, resulting from efficient sealing. Furthermore, the absence of anomalous soil CO_2 flux values on the top of the reservoir, except where the thermal spring discharges are located, can be explained by an effective cap-rock layer. Deep circulation of meteoric water, enriched with atmospheric gases, receives inputs of magmatic fluids (~11 % of primordial helium), leading to the development of the hydrothermal Na-Cl aquifer. However, this deep fluid contribution might be underestimated due to significant crustal assimilation (up to 50 %) involved in the magma genesis of the Cerro Galán Volcanic Complex, a process which modifies the He isotopic signature of the magmatic endmember. The hot springs, characterized by high flow rate (up to 459 m^3/h) are positioned at the intersection between the caldera margins and the NNE-SSW oriented tectonic structures, suggesting favorable permeability conditions. The preliminary geothermal gradient for the Cerro Galán area is estimated at around 98-101 °C/km. Such a high gradient can be attributed to the considerable heat flux generated by the transcrustal plumbing system of the Cerro Galán caldera, which includes the shallow crystal mush reservoir (<4 km depth). The preliminary geothermal potential of this giant caldera was performed using the volumetric method along with Monte Carlo simulations. The results indicate a probable power production capacity of 2.09 MWe and 10.85 MWe at 90 and 50 % confidence level, respectively. The results presented in this work constitute a foundational knowledge base to promote a more advanced exploration phase for the geothermal resource. Additionally to the local energy demand, lithium and other metal mining operations, which are operating independently from the National Interconnected System, could potentially be interested in power generation through binary cycles.

Keywords: *geothermal system - fluid geochemistry - geothermal prospection - large resurgent caldera - Southern Central Andes*

## 1. Introduction

The energy transition towards clean energy sources aimed to reduce the carbon footprint is already a worldwide fact. In this framework, the role of renewable energies as well as new renewable technologies aimed at net-zero emissions should be highlighted (e.g. Pfenninger et al., 2014; Gielen et al., 2019; Contino et al., 2020, Jolie et al., 2021; Sun et al., 2023; Buonomano et al., 2023). Nevertheless, in the global renewable matrix, including solar, wind, biomass, and hydro, the geothermal energy represents the smallest portion (around 1%; Krieger et al., 2022) due to different

barriers (mainly economic barriers related to the initial stages in exploration projects) that still exist for its use (e.g. Li et al., 2015; Colmenar-Santos et al., 2018; Witter et al., 2019; Pan et al., 2019; Palomo et al., 2022). Following this global trend, Argentina's policies promote the incorporation of renewable energies into the energy matrix through the National law N° 26.190/06. Despite Argentina having an estimated geothermal potential of 490-2010 MWe (Bona and Coviello, 2016), supported by the existence of encouraging geothermal systems for electric power generation (Chiodi et al., 2019; Barcelona et al., 2021, 2023; Filipovich et al., 2022), the only project that has reached the feasibility stage is the Copahue project (Japanese International Cooperation Agency; JICA, 1992). Therefore, the exploration of novel geothermal systems, mostly related to the generation of electrical power, plays a key role in incorporating new renewable sources into the energy matrix. Within the geothermal plays (Moeck, 2014), systems associated with volcanic calderas represent ideal targets for exploration (Goff and Janik, 2000; Giordano et al., 2014; Stimac et al., 2015). In this sense, the present investigation focuses on the giant Cerro Galán caldera (CGC), located in the Central Volcanic Zone of the Andes, as a major example of geothermal plays associated with volcanic calderas. Cerro Galán is a major Plio-Pleistocene resurgent caldera complex with more than 3.5 Myr of magmatic evolution (Sparks et al., 1985; Folkes et al., 2011a; Wright et al., 2011; Grocke et al., 2017), situated in the Southern Puna (~4,500 m a.s.l.; 25°49'S and 26°7'S-67°5'W and 66°51'W), NW Argentina (Fig. 1). Calderas with >10 km diameters require the accumulation of large volumes of silicic magma in the upper crust (e.g. de Silva and Gregg, 2014; Lipman and Bachmann, 2015; Kaiser et al., 2017), able to produce huge heat fluxes. Current evidence indicates the persistence of an anomalous thermal flux associated with the complex transcrustal magmatic system beneath the CGC (Delph et al., 2017; Ward et al., 2017). This is further supported by the presence of surface hydrothermal manifestations in the caldera area (Chiodi, 2015). In addition, despite the last caldera forming eruption occurred at 2.08 Ma (Cerro Galan Ignimbrite; Folkes et al. 2011a, b; Cas et al. 2011), recent reevaluation of the state of activity of Cerro Galan, based on its longevity and erupted volume suggest that the plumbing system may still be active (Giordano and Caricchi, 2022). The thermal features of the CGC consist of thermal springs from 25 °C to boiling point (~84 °C at 4,600 m a.s.l.), fumarolic discharges with temperatures up to 87.7 °C, argillic alteration zones, sinters, and travertine deposits (Chiodi, 2015). This paper presents and discusses the results of a detailed geochemical survey carried out in the hydrothermal manifestations in the Cerro Galán geothermal area in order to: (a) investigate the physicochemical conditions of the fluids into the geothermal reservoir(s), (b) define the primary sources of the fluids and the secondary processes controlling their chemistry, (c) propose the first hydrogeochemical conceptual model for the Cerro Galán geothermal system (CGGS) and (d) provide a preliminary estimation of the geothermal

100 potential aimed at evaluating the feasibility of using the geothermal resource according to the local

101 energy demand.

102
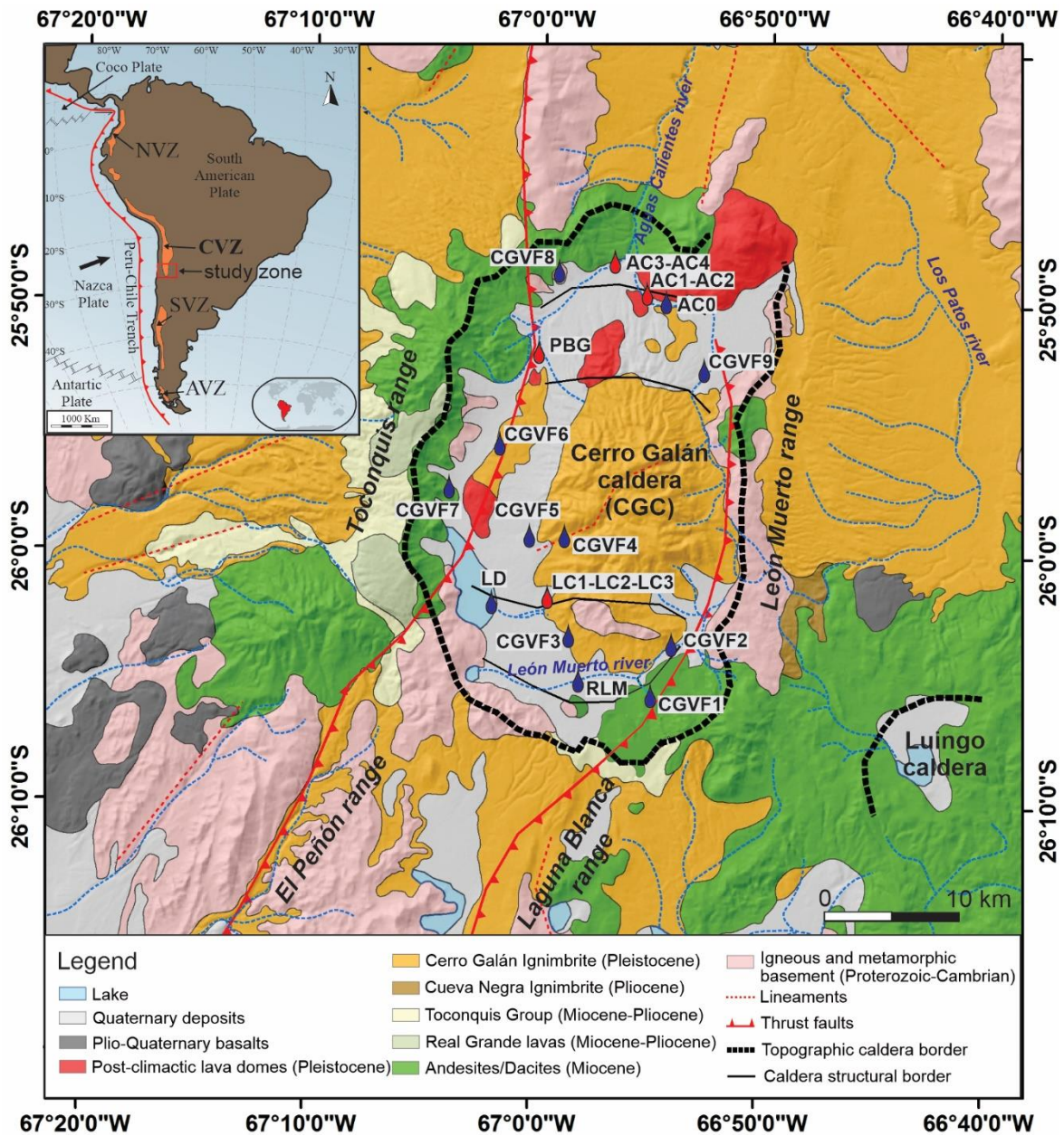
Fig. 1. Geological map of the Cerro Galán caldera area with the location of the sample sites (modified from Folkes et al., 2011a). NVZ: Northern volcanic zone. CVZ: Central volcanic zone. SVZ: Southern volcanic zone. AVZ: Austral volcanic zone. Red drop: sample location (hydrothermal manifestation). Blue drop: sample location of stream/cold spring/lake.

2. Geological setting

2.1. Stratigraphy and volcanological features

The magmatic evolution of the Andes fluctuated between long-term steady-state phases dominated by andesitic-dacitic stratovolcanoes and episodic high-flux flare-up events producing large caldera-

forming eruptions and huge volumes of dacitic-rhyolitic ignimbrites (DeCelles et al., 2015; de Silva and Kay, 2018). The paradigmatic example of this arc dynamic is the Neogene Ignimbrite Province of the Central Andes (NIPCA, de Silva and Kay, 2018). The NIPCA records a diachronic flare-up event developed in response to the progressive slab re-steepening accompanying the southward migration of the Juan Fernandez aseismic ridge during the last 25 Ma (Kay and Coira, 2009; Freymuth et al., 2015). The youngest large caldera system related to this time-transgressive regional process is the Cerro Galán Volcanic Complex (~5.6-2.0 Ma) located in the southern edge of the NIPCA, in the Southern Puna region (Friedman and Heiken, 1977; Francis and Baker, 1978; Sparks et al., 1985; Francis et al., 1983; Folkes et al., 2011a, b, c; Kay et al., 2011; Grocke et al., 2017). The Cerro Galán Volcanic Complex (CGVC) produced at least nine ignimbrites, with the youngest being the Cerro Galán Ignimbrite (~2 Ma; ~630 km^3 DRE), the climactic event responsible for the present CGC (Folkes et al., 2011a). The CGC is a major (27×16 km) trapdoor caldera whose collapse was controlled by a N-S fault located at its eastern side which acted as a hinge producing an asymmetric collapse that accommodated a minimum intracaldera ignimbrite thickness of ~1.5 km (Folkes et al., 2011a). The N-S fault-oriented system controlling the caldera collapse is part of the first-order structural architecture of the Southern Puna which was developed in response to the compressional tectonics during the Cenozoic evolution of the Central Andes (Báez et al., 2023 and reference therein). The second order W-E structures controlled the differential subsidence of blocks (picemeal collapse). The CGVC was preceded by a Miocene meso-siliceous volcanism developed above a complex igneous-metamorphic Neo-proterozoic/Paleozoic basement (Francis et al., 1983; Hongn et al., 2001). The CGC recorded an important resurgence of the caldera floor in response to the rise of the remaining magma to very shallow levels (< 4 km), which was also extruded forming post-caldera lava domes and block and ash flow deposits (Grocke et al., 2017).

The CGVC was fed by a transcrustal long-lived magmatic system characterized by deep MASH zone located in the lower crust that acted as buffering "zone" between the mantle source and the upper crust reservoirs (Folkes et al., 2011b; Kay et al., 2011). Melts extracted from the MASH zone stalled in the middle crust (~20 km) forming a large magma body that episodically delivered more evolved melts to the upper crust where they were stored and forming large shallow (10-5 km) mush-type reservoirs. These shallow reservoirs were episodically mobilized during the eruption of the crystal-rich ignimbrites of the CGVC (Folkes et al., 2011b; Kay et al., 2011). The upper crustal reservoirs became progressively shallower during the evolution of the CGVC, being the climactic CGI eruption and the post-caldera activity sourced by a reservoir located at < 4 km deep (Folkes et al., 2011b; Wright et al., 2011; Grocke et al., 2017).

Several geophysical surveys (Bianchi et al., 2013; Calixto et al., 2013; Heit et al., 2014; Liang et al., 2014, Delph et al., 2017; Ward et al., 2017) have imaged a large ($\sim$22,000 km^3) partial melting zone in the middle crust (16-28 km deep) under the CGVC, known as the "Cerro Galan magma body" (Delph et al., 2017; Ward et al., 2017). In addition, a deeper geophysical anomaly (partial melting zone) located at the crust-mantle boundary, was identified in this region (Delph et al., 2017; Ward et al., 2017). Both geophysical anomalies match with the petrologically inferred MASH zone and middle crustal main reservoir that fed the CGVC (Folkes et al., 2011b; Kay et al., 2011). This implies that the transcrustal feeder system is still active and that the CGVC can be defined as a very long-quiescent dormant volcano (Giordano and Caricchi, 2022). In this sense, the short-duration seismic swarms that occurred on January 25, 2009 under the Galán resurgent dome are probably reflecting shallow hydrothermal fluid or magma movement (Mulcahy et al., 2014). Furthermore, the current anomalous thermal state of the crust and shallow brittle-ductile transition below the CGVC is evidenced by its prevailing shallow (< 5 km) and low magnitude (< 3 M$_c$) seismicity (Mulcahy et al., 2014).

2.2 Hydrothermal manifestations

There are three main sectors with hydrothermal manifestations in the CGC, as follows (Fig.1, 2): a) La Colcha area (LC), situated on the southern border of the resurgent dome; and b) the Aguas Calientes area (AC) and c) the Piscinas Burbujeantes del Galán (PBG), the two latter being located toward the N-NW structural border of the CGC.

a) La Colcha area (LC; Fig. 1,2) consists of several hot springs spreading in a narrow area ($\sim$3 km^2), which emerge from the CGI with Na-Cl composition and temperature up to 83.9 °C. The hot springs runoff forms a creek ($\sim$288 m^3/h) that is tributary to the Diamante Lake (Fig. 2a). In the surroundings of the hot springs, there is a phreatic explosion crater (Fig. 2b) and travertine domes (Fig. 2b,c,d) suggesting a more intense hydrothermal activity in the past. There is a significant salt deposition on the soil in all the hot springs area (Fig. 2c,e), mainly consisting of calcite and halite (Massenzio et al., 2023, 2024).

b) Aguas Calientes area (AC; Fig. 1,2) is a group of springs located near the northern border of the CGC, associated with a NW-SE fault system, in a ravine where the Aguas Calientes river flows to finally turn toward north running out of the CGC area (Figs. 2f,g). The hot springs, characterized by a Na-Cl composition and temperature up to 61 °C, discharge $\sim$765 m^3/h to the Aguas Calientes river. Most hot springs are issuing from fluvial deposits that infill the ravine and some of them emerge at the contact between these deposits and a block- and ash-flow deposit (Figs. 2g,h). There is also deposition of salts on the soil surface (Fig. 2i).

Fig. 2. (a) Satellite image (Google Earth data) of the La Colcha hot springs area and (b) a detailed map indicating sampling

and measurement sites. (c) View of the LC1 sample site, with the travertine dome elevated topographically in relation to

the current thermal springs. (d) Detailed photograph of the travertine. (e) View of the LC3 sample site. (f) Satellite image

183 (Google Earth data) of the Aguas Calientes hot springs area and (g) a detailed map showing the sampling and measurement

184 sites. Detailed photographs of the AC1 sample site (h) and AC2 sample site (i).

185

186 *c) Piscinas Burbujeantes del Galán (PBG; Figs. 1,3)* consists of geothermal fumaroles and acid-

187 sulphate bubbling pools located on the western structural border of the CGC. The fumaroles have

188 temperatures up to 87.7 °C while those of the bubbling pools are up to 80 °C. In the topographically

189 higher sectors, siliceous sinter deposits and fragments of the altered and silicified CGI have been

190 identified (Figs. 3a,b). The entire PGB area is characterized by intense hydrothermal alteration,

191 particularly in the vicinity of the fumarolic vents (Fig. 3c). Kaolinite, hematite, boehmite and sulphates,

192 among other minerals, have been identified in this area (Massenzio et al., 2023, 2024).

193
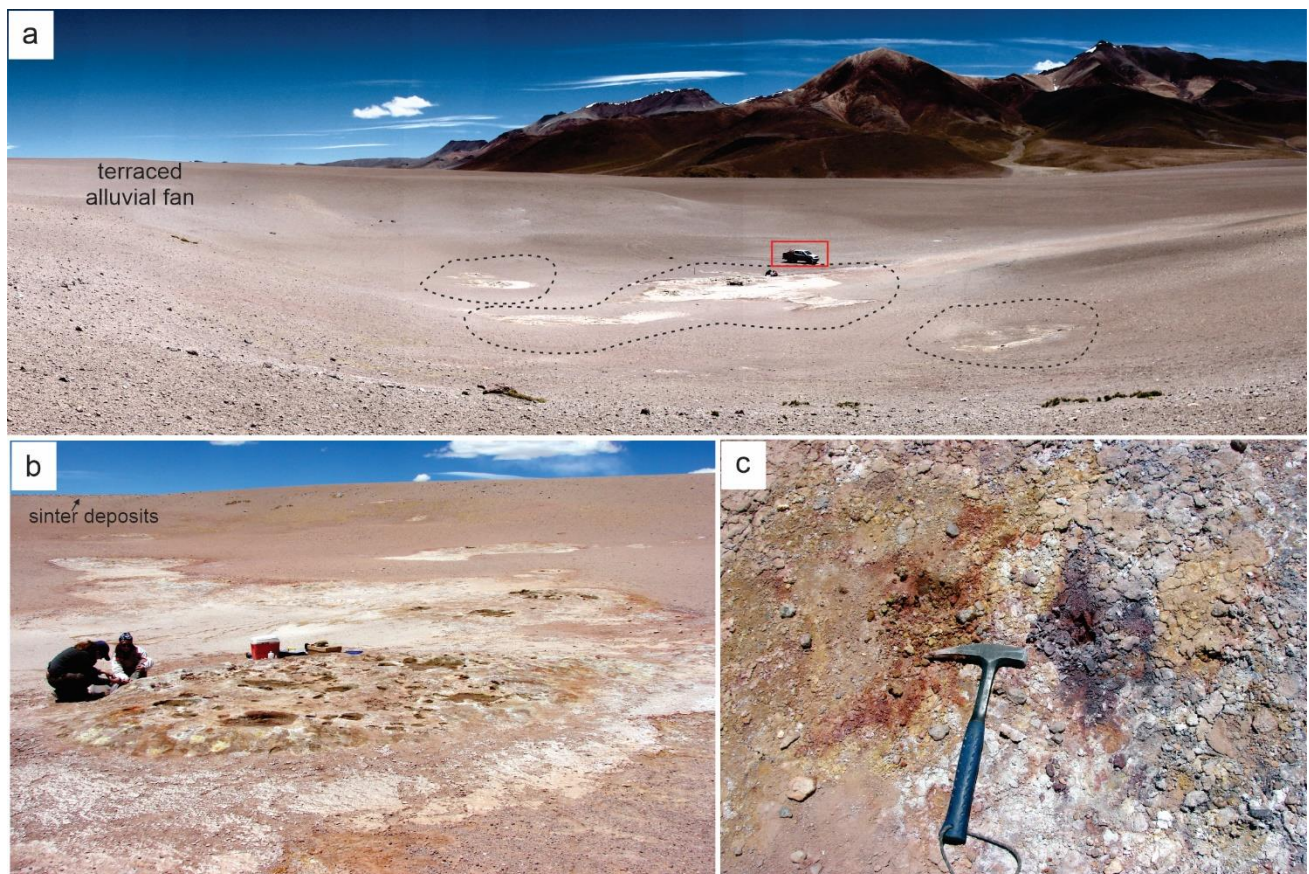
194

195 Fig. 3. (a) Panoramic view (toward W) of the Piscinas Burbujeantes del Galán geothermal area. (b) General view of the

196 PBG sample site and the alteration zone. (c) Detailed view of the hydrothermal alteration minerals.

197

198 3. Methods

199 **3.1. Sampling sites and methods**

200 Nineteen water samples from 6 hot springs (AC1, AC3, PBG, LC1, LC2, LC3), 9 cold springs

201 (CGVF1, CGVF2, CGVF3, CGVF4, CGVF5, CGFV6, CGVF7, CGVF8, and CGVF9), 2 creeks (AC0

and RLM), 1 salt lake (LD) and 1 snow sample (CGN) were collected at the CGC. Water temperature, pH and electrical conductivity (EC) were measured at each sample point using a multiprobe instrument (*Hanna HI 98195*; accuracy: ±0.15 °C, ±0.02 and ±1 %, respectively). Total alkalinity (expressed as mg/L CaCO$_3$) and silica were analyzed *in situ* by (i) acidimetric titration using HCl 0.03 N, phenolphthalein and bromophenol blue as indicators, and (ii) molecular spectrophotometry (*Hanna HI 96770C*; accuracy: ±1 mg/L), respectively. The chemical-physical parameters determined in the field are reported in Table 1. From each sampling point, three aliquots of water were collected in high-density polyethylene bottles, as follows: i) 1 filtered sample (0.45 µm filter pore size) for the analysis of major cations and anions, ii) 1 filtered sample (0.45 µm filter pore size) acidified with ultrapure HNO$_3$ for the analysis of trace elements, and iii) 1 unfiltered sample for the analysis of water isotopes and finally, iv) 1 filtered sample (0.45 µm filter pore size) acidified with 1% (v/v) HCl 6 N and stored in dark bottles for the analysis of As(III) and As(V).

Bubbling gases from AC1, PBG, and LC1 were sampled using a plastic funnel up-side-down positioned above the bubbles and connected through tygon tubes to the sample flasks. For the determination of the gas chemical composition, pre-evacuated 60 mL glass thorion tapped bottles filled with 20 mL of a 4 N NaOH solution were used (Giggenbach and Goguel, 1989), whereas the carbon isotopic ratio in CO$_2$ was analyzed in gases stored in pre-evacuated 60 mL flasks (Vaselli et al., 2006). Samples for the analysis of dissolved gases were (AC1 and LC1) were collected in 50 mL glass flasks equipped with a rubber septum. In the laboratory, the method proposed by Chiodini (1996), slightly modified, was applied by determining the chemical composition according to the measured based on pressure, volume of concentrations of gases stored in the headspace of the flasks created by injecting Ar and/or He (Whitfield, 1978).

3.2. Chemical and isotopic analyses of water samples

Major cations (Na$^+$, K$^+$, Ca^{2+}, Mg^{2+}, Li$^+$, and NH$_4^+$) and anions (F$^-$, Cl$^-$, SO$_4^{2-}$, Br$^-$, and NO$_3^-$) were analyzed by ion-chromatography (IC: *Eco IC Metrohm*). The analytical error was ≤ 5%. Boron was analyzed by molecular spectrophotometry (MS: *Beckman DU 520*) using the Azomethine-H method (Bencini, 1985). The analytical error was ≤ 5 %.

Trace elements were analyzed by Inductively Coupled Plasma Mass Spectrometry (ICP-MS: *ELAN-DRC Perkin Elmer spectrometer*). The analytical error is ≤ 10 %. Total arsenic (AsT) was analyzed by Inductively Coupled Plasma Mass Spectrometry analysis (ICP-MS: *Perkin-Elmer SCIEX, ELAN DRC-e*) and the inorganic species (As(III) and As(V)) were analyzed by anion exchange chromatography (AEC) employing a chromatographer (*Series 200, Perkin-Elmer*) with ICP-MS determination.

235 The $^{18}O/^{16}O$ and $^{2}H/^{1}H$ ratios in water (expressed as δ^{18}O–H$_2$O and δ^{2}H-H$_2$O ‰ vs. V-SMOW,

236 respectively) were analyzed using an Ultra High-Precision Isotopic Water Analyzer *Picarro L2130-i*

237 laser spectrometer. The analytical errors for δ^{18}O–H$_2$O and δ^{2}H-H$_2$O values are ±0.25 ‰ and ±1.20

238 ‰, respectively.

239

240 ### 3.3. Chemical and isotopic analysis of dissolved and bubbling gases

241 Inorganic gases (N$_2$, O$_2$, H$_2$, CO, Ar, Ne, and He) in the headspace of the soda flasks, as well as those

242 collected in the headspace of the dissolved gas vial (N$_2$, O$_2$, CO, Ar, He, Ne, CO$_2$, and H$_2$S), were

243 analyzed by gas chromatography (GC: *Shimadzu 15A*, equipped with a Thermal Conductivity

244 Detector). Carbon dioxide and H$_2$S in the alkaline solution were analyzed as CO_3^{2-}, by acidimetric

245 titration with a HCl 0.1 N solution, and SO_4^{2-}, by IC after oxidation with H$_2$O$_2$, respectively. Methane

246 and light hydrocarbons were determined by gas chromatography (GC: *Shimadzu 14A,* equipped with

247 a 10-m-long stainless-steel column packed with Chromosorb PAW 80/100 mesh coated with 23 % SP

248 1700 and a Flame Ionization Detector). The analytical errors for GC analyses were ≤ 5%. The $^{13}C/^{12}C$

249 ratios of CO$_2$ and CH$_4$ (in LC1) (expressed as δ^{13}C-CO$_2$ and δ^{13}C-CH$_4$ ‰ vs. V-PDB) were measured

250 by Cavity Ring Down Spectroscopy (CRDS) using a *Picarro 2201-i* instrument. The analytical error

251 was ±0.1 ‰, respectively. The helium isotopic ratios (expressed as R/Ra, where R is the $^{3}He/^{4}He$ ratio

252 measured in the sample and Ra is the same ratio in the air and equal to 1.39×10^{-6}; Mamyrin and

253 Tolstikhin, 1984) and those of $^{4}He/^{20}Ne$ were determined by using a double collector mass

254 spectrometer (*Helix SFT-GVI*) and a multicollector *Helix MC Plus Thermo*, for helium and neon

255 isotopes respectively, according to the method described by Rizzo et al. (2015, 2016). The analytical

256 error was generally < 2%. Air standard aliquots were used as internal reference to normalize the R/Ra

257 values. The R/Ra values were corrected for atmospheric contamination using the $^{4}He/^{20}Ne$ ratios

258 (Poreda and Craig, 1989), as follows:

259

260 $\qquad$ Rc/Ra = [(R/Ra$_{measured}$) − r]/(1 − r) $\hfill$ (1)

261

262 where r is ($^{4}He/^{20}Ne$)$_{air}$/($^{4}He/^{20}Ne$)$_{measured}$ and that of ($^{4}He/^{20}Ne$)$_{air}$ is 0.318 (Ozima and Podosek, 1983).

263

264 ### 3.4. Lineament analysis

265 The distribution and density of tectonic lineaments were analyzed to assess areas showing surface

266 evidence of reservoir permeability. Lineaments were semi-automatically detected over an area of

267 approximately 5,000 km^2 using an ALOS PALSAR Digital Elevation Model (DEM) from the Alaska

268 Satellite Facility (https://earth.esa.int/eogateway/catalog/alos-palsar-products) with a spatial

269 resolution of 12.5 m. Shaded relief images were created from eight different azimuths (0°, 45°, 90°,

270 135°, 180°, 235°, 270°, and 315°) to highlight all lineaments, considering that the visible of relief

271 linear features are influenced by lighting conditions (Wise et al., 1985). Identification, mapping, and

272 analysis of lineaments were carried out according to the methodology proposed by Giordano et al.

273 (2013; 2014). The areal density and azimuth of lineaments were also calculated. The lengths of the

274 lineaments were assessed through cumulative frequency distribution. Frequency distributions of both

275 regional and local lineaments were calculated, as well as those of structures located within the different

276 recharge areas.

277

278 ## 4. Results

279 ### 4.1. Chemical and stable isotopic ($\delta^{18}O$ and $\delta^{2}H$) composition of waters

280 As shown in the classification diagrams reported in Fig. 4a,b, most cold spring have a Na^+-HCO_3^-

281 composition, La Colcha and Aguas Calientes waters are Na^+-Cl^- type, whereas CGVF8 and PBG are

282 the only Ca^{2+}-Cl^- and Na^+-SO_4^{-2} waters, respectively.

283 La Colcha and Aguas Calientes thermal waters have a slightly acidic to near neutral pH range of 6.08

284 to 7.11, outlet temperatures and TDS (Total Dissolved Solids) ranging from 21.3 to 83.9 °C, and from

285 1,460 to 3,100 mg/L, respectively. These waters are also characterized by high concentrations of SiO_2

286 (up to 207 mg/L), B (up to 75.1 mg/L), Li^+ (14.1 mg/L) and Br^- (up to 10.8 mg/L) (Table 2), as well

287 as of As (up to 11300 µg/L), Mn (198 µg/L), Sb (199 µg/L), Se (6.5 µg/L), Ba (14 µg/L), Zn (15 µg/L),

288 and Cu (8.4 µg/L) (Table 3; Fig. 4c).

289 PBG has an outlet temperature of 80 °C, acidic pH (4.95), low TDS (218 mg/L), and trace element in

290 concentrations comparable to those of the Na^+-Cl^- waters (Fig. 4c), except for As, which shows a lower

291 concentration (up to 140 µg/L).

292 The oxygen and hydrogen isotopic data of the thermal waters vary from -7.7 to -1.6 and from -55 to -

293 51 ‰ vs. V-SMOW.

294 Cold waters having Na^+-HCO_3^- composition (RLM, CGVF1, CGVF3, CGVF4, CGVF7, and AC0).

295 show temperatures and TDS ≤19.7 °C and ≤765 mg/L, respectively, and a slightly acidic pH (from

296 5.66 to 6.84). The two Na^+-Cl^- cold waters (CGVF6 cold spring and LD, salt lake) exhibit pH values

297 of 6.7 and 9.2, respectively, whereas their TDS values are 681 mg/L and 270,305 mg/L, respectively.

298 The Ca^{2+}-Cl^- cold water (CGVF8) is characterized by low temperature of 4.9 °C, a slightly acidic pH

299 of 6.09, and a low TDS value of 434 mg/L. LD waters shows relatively high concentrations in trace

300 elements (Table 3): As (up to 342,330 µg/L) and Cu (306 µg/L), which are significantly higher than

301 those observed in the thermal waters, followed by Fe (72 µg/L), Ba (35 µg/L), Al (17 µg/L), Mn (8.5

302 μg/L) and Zn (7.4 μg/L). The $\delta^{18}O$-H_2O and δ^2H-H_2O values (Table 2) of the cold waters ranges from

303 -8.90 to -2.7 ‰ and from -53 to -31 ‰ vs. V-SMOW, respectively.

304 The $\delta^{18}O$-H_2O and δ^2H-H_2O values of the snow sample (GCN) are in the range of those measured in

305 the cold waters, being -7.69 ‰ and -38 ‰, respectively (Table 2).

306

4.2. Chemical and stable isotopic ($\delta^{13}C$-CO_2 and R/Ra) composition of gases

308 The chemical composition of the bubbling and dissolved gases is shown in Table 4 (in mmol/mol),

309 along with the $\delta^{13}C$-CO_2, $\delta^{13}C$-CH_4, Rc/Ra, and $^4He/^{20}Ne$ values.

310 The chemical composition of the bubbling gases is dominated by CO_2 (from 851 to 879 mmol/mol),

311 followed by N_2 (up to 141 mmol/mol), H_2S (up to 1.3 mmol/mol), CH_4 (up to 0.22 mmol/mol), H_2 (up

312 to 0.018 mmol/mol), and He (up to 0.0105 mmol/mol). Carbon monoxide was below the analytical

313 detection limit (0.001 mmol/mol). Atmospheric gases (O_2, Ar, and Ne) are present at low

314 concentrations, up to 5.61, 3.31, and 0.0018 mmol/mol, respectively. Light hydrocarbons also occur

315 at low concentrations, mainly consisting of ethane (C_2H_6, up to 0.0031 mmol/mol) and benzene (C_6H_6,

316 up to 0.0015 mmol/mol). The $\delta^{13}C$-CO_2 values vary within a relatively narrow range: from -9.25 ‰ to

317 -6.51 ‰ vs. V-PDB. The $\delta^{13}C$-CH_4 was only measured in AC1 with a value of -31.8 ‰ vs. V-PDB.

318 The Rc/Ra values range from 0.27 to 0.96 with $^4He/^{20}Ne$ between 2 and 5.8.

319 Gases dissolved in the thermal waters are mainly consisting of N_2 (ranging from 549 to 669 mmol/mol)

320 and CO_2 (from 157 to 300 mmol/mol), with low concentration of CH_4 and He (up to 0.005 and 0.0021

321 mmol/mol, respectively). Oxygen, Ar and Ne exhibit relatively high concentrations, reaching up to

322 158, 16 and 0.0083 mmol/mol, respectively. Carbon monoxide, H_2S, H_2 and light hydrocarbons were

323 not detected.

324

325
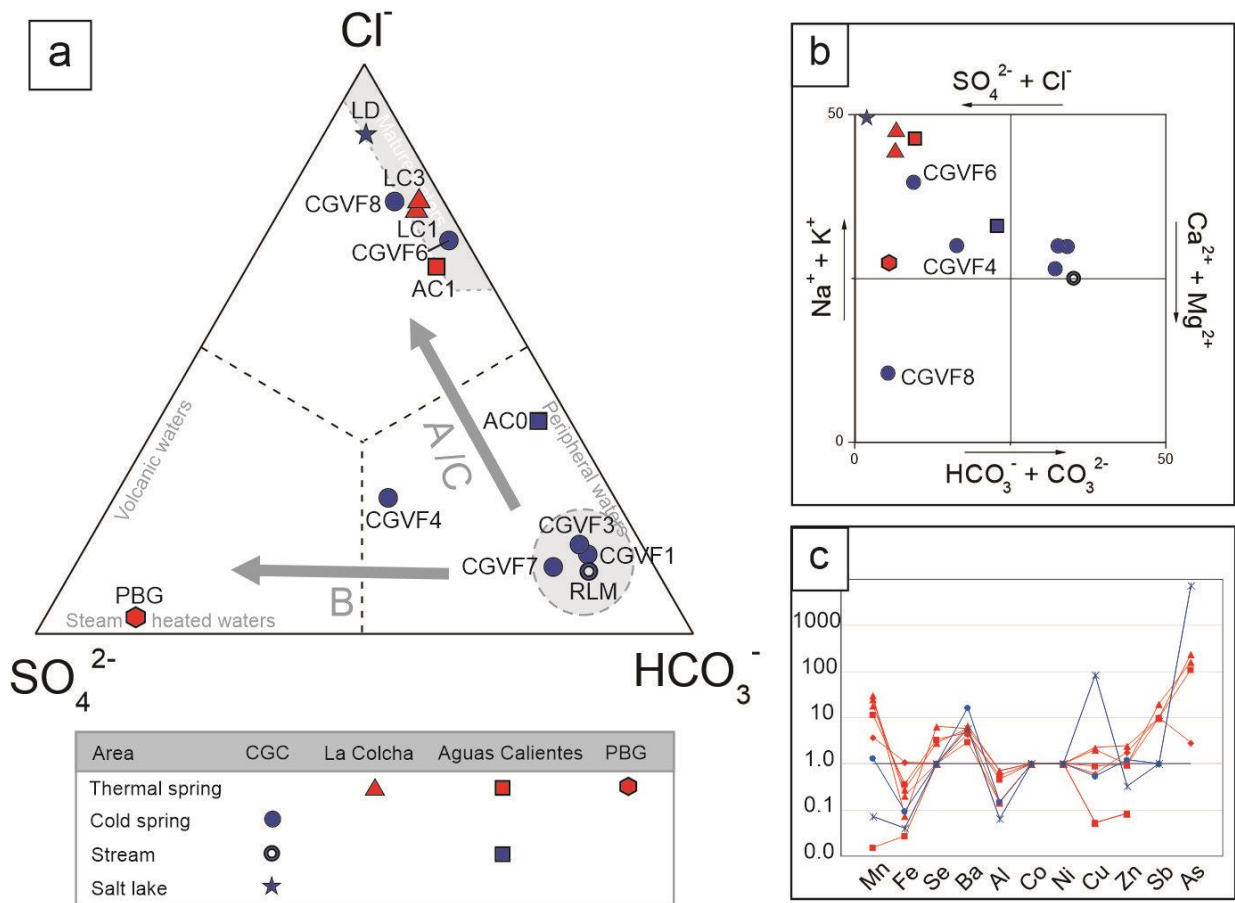
Fig. 4. (a) HCO_3^--Cl^--SO_4^{-2} ternary diagram and (b) Square diagram for the cold and thermal waters from the CGGS (in mg/L). (c) Trace element diagram normalized to RLM for the cold and thermal waters from the CGGS (in µg/L).

4.3. Density and azimuth of lineaments

The lineament analysis successfully identified 803 lineaments with lengths ranging from 200 to 18,000 m (Fig. 5). The arithmetic average lineament length is approximately 2,300 m. The highest lineament densities are concentrated in the area of the resurgent dome and towards the topographic borders of the CGC (Fig. 5). Lineaments situated on the caldera floor, surrounding the resurgent dome, could possibly be buried by the still active deposition of alluvial fans (low-density area, Fig. 1 and 5).

The azimuthal frequency of the lineaments was statistically analyzed using rose diagrams. The most frequent azimuthal orientation is NW-SE, with subordinate orientations being NNE-SSW and NE-SW (Fig. 5a). Analyzing the lengths of the lineaments, a change in the curvature of the distribution at 4,000 m length defined two populations (90 % cumulative frequency): long lineaments (>4,000 m; n=91) and short lineaments (<4,000 m; n=712) (Fig. 5b). The frequency of lineament directions shows that the NW–SE is significant for the shorter lineaments (<4,000 m; Fig. 5c), although lineaments are

present in most of the azimuthal directions. Lineaments longer than 4,000 m have preferential azimuths in NNE-SSE and NW-SE (110°-120°; 130-140°; Fig. 5d).
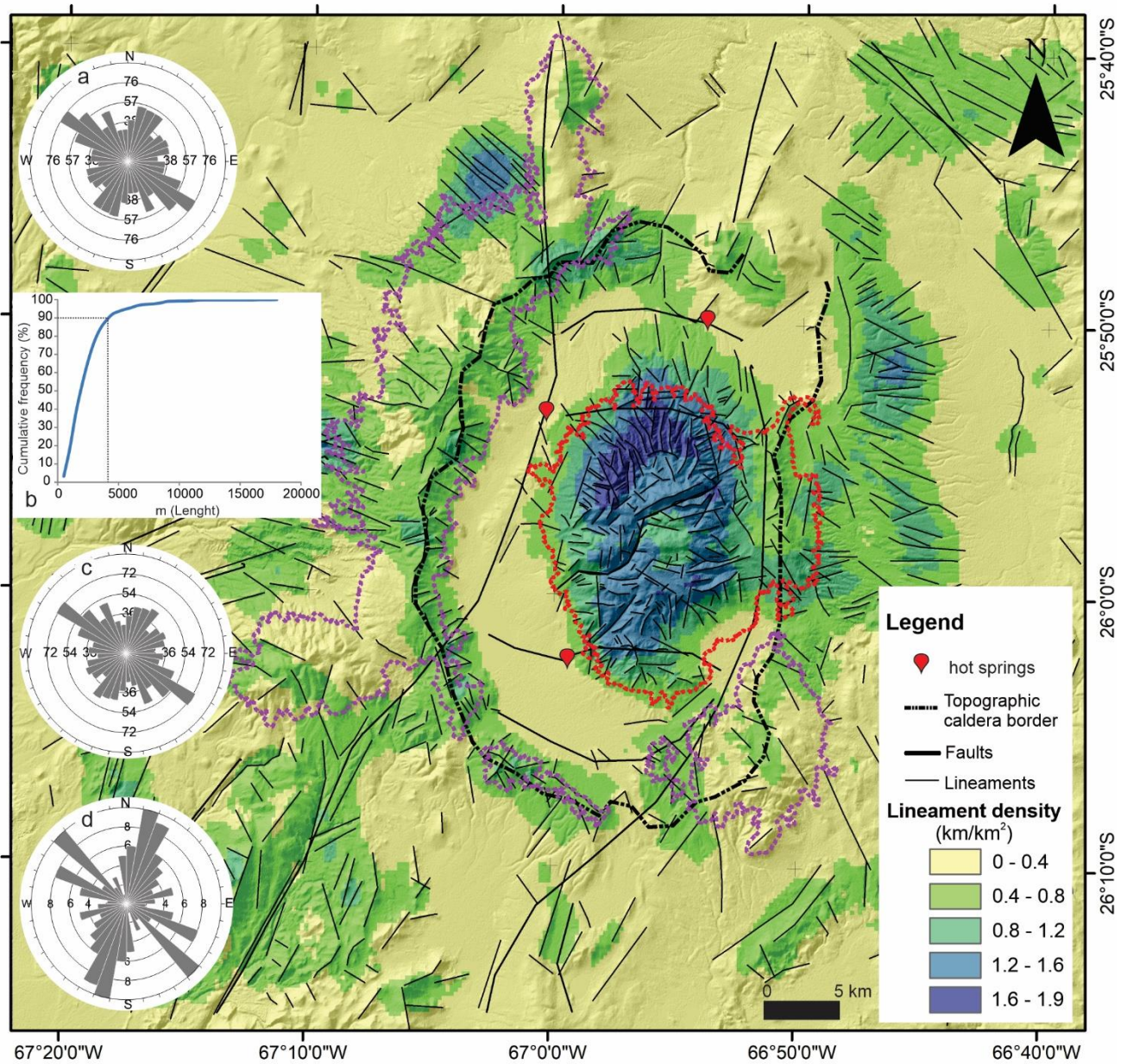

Fig. 5. Map of lineaments at Cerro Galán area showing lineament densities. (a) Rose diagram showing the frequency distribution of the orientation for the identified lineaments. (b) Cumulative frequency distribution of lineaments length. The black dotted line shows the change in the distribution at 4,000 m (90%). (c) Rose diagram showing the frequency distribution of the orientation for lineaments <4,000 m. (d) Rose diagram showing the frequency distribution of the orientation for lineaments >4,000 m. Purple dotted line represents the contour of 4,850 m, indicating the main recharge area of the deep aquifer. The red dotted line represents the contour of 4,850 m, indicating the main recharge area for the shallow aquifer.

354 5. Discussion

355 5.1. Origin of waters

356 The isotopic composition, expressed as $\delta^{18}O$-H_2O and δ^2H-H_2O ‰ vs. V-SMOW, indicates a meteoric

357 origin for all the waters (Fig. 6). However, most CGGS water samples slightly deviate from the Local

358 Meteoric Water Line (LMWL: $\delta^2H = (8.01 \pm 0.08) \delta^{18}O + (15.2 \pm 0.7)$ ‰: Gonfiantini et al., 2001),

359 suggesting an evaporative process typical of high-altitude hyper-arid environments (Fiorella et al.,

360 2015; Bershaw et al., 2016). Similar observations have indeed been recorded in other geothermal

361 system closer to the CGGS, such as the Cerro Blanco geothermal system (CBGS; Chiodi et al. 2019;

362 Fig. 6), as well as in stream waters across the Andean Plateau (Bershaw et al., 2016). A positive

363 isotopic shift in $\delta^{18}O$, attributed to water-rock isotopic exchange at relatively high temperatures (> 150

364 °C; Truesdell and Hulston, 1980), cannot be ruled out for the thermal waters. The PBG sample

365 constitutes a particular case, as its shift (Fig. 6) can be explained in terms of an extensive surface

366 evaporation process (Craig et al., 1963), similar to that observed in acid-sulfate steam-heated pools at

367 El Tatio (Giggenbach, 1978).

368
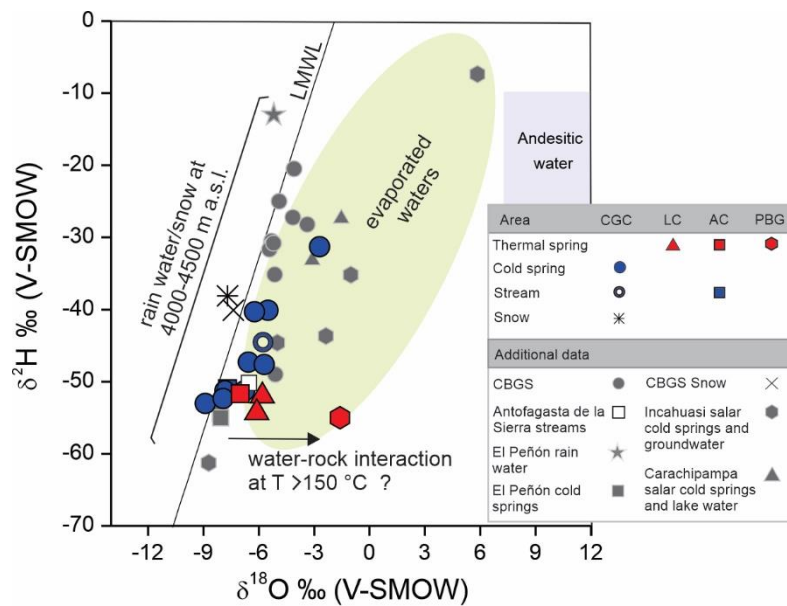
370 Fig. 6. $\delta^{18}O$-H_2O and δ^2H-H_2O binary diagram for cold and thermal waters from the CGGS. The Local Meteoric Water

371 Line (LMWL: $\delta^2H = (8.01 \pm 0.08) \delta^{18}O + (15.2 \pm 0.7)$ ‰: Gonfiantini et al., 2001), is also shown. Additional isotopic data

372 is provided for comparison (Supplementary material): hot and cold springs, and a snow sample from the Cerro Blanco

373 geothermal system (CBGS); the mean value of the Antofagasta de la Sierra streams, located near the western edge of the

374 CGC, cold springs and rain water from the El Peñón town, located ~45 km southwest of the CGC; cold springs and lake

375 water from the Carachipampa Salar, located ~62 km southwest of the CGC; and cold springs and groundwater from the

376 Incahuasi Salar, located ~75 km southwest of the CGC.

377

378   According to the ternary diagram of Fig. 4a, the distribution of both cold and hot waters suggests the

379   contribution of various processes controlling the water chemistry. Further indications on these

380   processes are provided by the binary plots in Figs. 7 and 8, where the LC and AC thermal waters show

381   chemical-physical features, e.g. high temperature and TDS (trend A; Fig. 7) and Na^+/Cl^- mol ratios

382   ~1 (Fig. 8a), which are consistent with those expected for typical geothermal brines (e.g. Giggenbach,

383   1997). The PBG thermal water depict a different trend (B), having a high temperature (80 °C) and a

384   low TDS (218 mg/L) (Fig. 7) and being characterized by a (SO_4^{2-})/$(Ca^{2+}+Mg^{2+})$ mol-ratio >>1 (10.4;

385   Fig. 8b). Such chemical features suggest that this water is a typical heated steam, i.e. a surficial water

386   whose relatively high SO_4^{2-} contents are due oxidation of H_2S from gases similar to those occurring as

387   bubbling phase in the LC and AC thermal waters (Table 4). Due to steam condensation, which

388   dissolves some of the more soluble gases such as ammonia, boron, and arsenic, removing them from

389   the vapor (e.g. Nicholson, 1993; Tassi et al., 2005), the relatively high NH_4^+ concentration in PGB

390   (Table 1) confirms the origin of this water. Carbonate dissolution and interaction of waters with CO_2

391   are likely the main sources for HCO_3^- and CO_3^{2-} in most of the studied waters (Fig. 8c). Addition of

392   Na^+ released in waters by hydrolysis of Na-silicates (e.g. feldspars and their alteration products), can

393   explain the Na^+ excess exhibited by the thermal waters (Fig.8d), a process favored by the presence of

394   CO_2 and H_2S (Table 4). The hypersaline cold water of the LD sample (Fig. 7), characterized by a

395   Na^+/Cl^- mol ratio ~1 (Fig. 8a), depicts a third trend (C) likely attributed to the evaporation process.

396   The Diamante Lake (LD) constitutes a closed drainage system that receives sporadic runoff water (low

397   TDS and Na^+-HCO_3^- type), from the SW sector of the CGC, in addition to the continuous input of

398   thermal waters from the La Colcha area (LC; Fig. 1), which is then subjected to intense evaporation.

399    $Ca^{2+}+Mg^{2+}$ depletion due to precipitation of carbonate rocks, whose presence was recognized in the

400   Diamante Lake (Stepanenko et al., 2020), explains the high (SO_4^{2-})/$(Ca^{2+}+Mg^{2+})$ mol-ratio of this

401   sample (Fig. 8b). Such an alkaline lagoon (pH = 9.20) can be classified as a typical Soda Lake (Jones

402   and Grant, 1999; Ma et al., 2004; Kulp et al., 2008; Pecoraino et al., 2015).

403
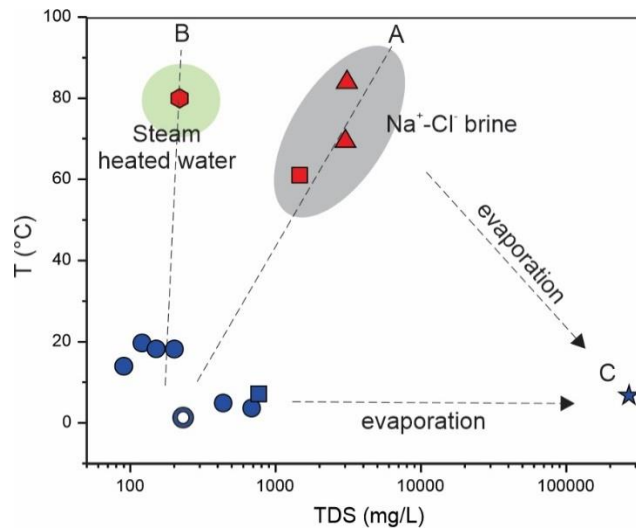
Fig. 7. Total Dissolved Solids (TDS) vs. temperature (T) binary plot for the cold and thermal waters from the CGGS. The symbols as in Fig. 4.
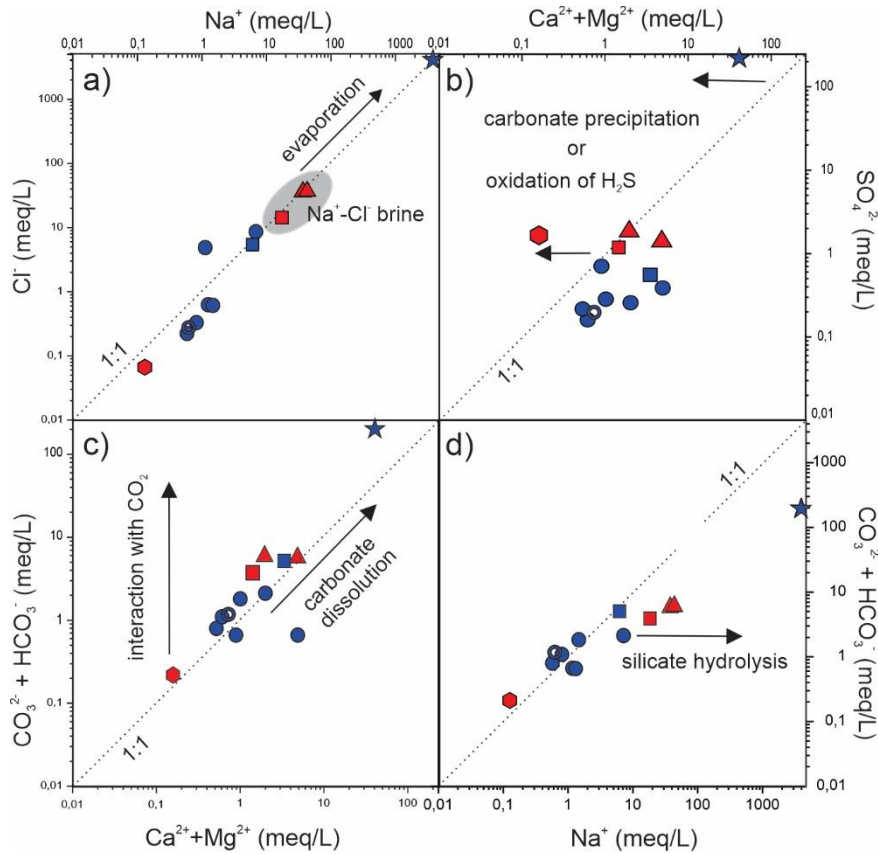
Fig. 8. (a) Cl^- vs. Na^+, (b) SO_4^{2-} vs. $Ca^{2+}+Mg^{2+}$, (c) $CO_3^{2-}+HCO_3^-$ vs. $Ca^{2+}+Mg^{2+}$, and $CO_3^{2-}+HCO_3^-$ vs. Na^+ binary diagrams for the cold and thermal waters from the CGGS. The symbols as in Fig. 4.

Among trace elements, it is worth noting the high concentrations of As in both thermal waters and cold waters, with levels reaching up to 11,340 and 342,330 µg/L AsT, respectively (Fig. 4c, Table 3). The

415   Altiplano-Puna plateau area (CVZ) is characterized by a high As-background in both geothermal fluids

416   (e.g. Chiodi et al., 2019; Filipovich et al., 2022) and surface waters (e.g. Tapia et al., 2019; Sanci et

417   al., 2020), mainly due to water-rock interaction processes (Murray et al., 2023). Particularly, collapse

418   calderas and ignimbrites fields from the Altiplano-Puna region have a mean As concentration of 7.3

419   mg/kg, approximately 2 times higher than that of the upper continental crust (Murray et al., 2023).

420   Therefore, leaching of the host rocks can explain the very high arsenic concentrations measured in the

421   waters of CGC. Additionally, once that As was released from the rocks, the very arid climate

422   conditions and the presence of alkaline water further favor the accumulation of As (Murray et al.,

423   2023). The aforementioned factors could explain the exceptionally high concentration of As analyzed

424   in the Diamante lake (LD sample, Table 3). In addition to these sources and processes, As in the

425   thermal waters may also be ascribed, at least partially, to inputs of deep-originated fluids of magmatic

426   origin, which are commonly rich in this element (e.g. Webster and Nordstrom, 2003; Lopez et al.,

427   2012). As far as the As speciation is concerned, arsenite (H_3AsO_3) is the predominant species in

428   thermal waters, with concentrations ranging from 4 to 3,070 μg/L iAs(III), being particularly high in

429   the Na-Cl waters from LC and AC hot springs areas. In cold waters, arsenate ($H_2AsO_4^-$) turns to be the

430   main species, with concentrations ranging from 5 to 276,740 μg/L iAs(V). This change in arsenic

431   species is likely due to an increase in redox potential and oxidative conditions of the cold waters

432   (Farnfield et al., 2012). This is consistent with the higher Eh value measured in the Diamante Lake

433   (159.8 mV) in comparison to the reductive values determined in La Colcha thermal waters (48.3 and

434   1.9 mV), the main thermal affluent to the lake (Tables 1 and 3). In addition, in Laguna Diamante, the

435   existence of microorganism capable to oxidize As(III) to As(V) and precipitate both in living

436   microbialites mats (Sancho-Tomás et al, 2020) could contribute to the consumption of As(III) from

437   the solution.

438   Figure 9 illustrates the Li^+, B and Cl^- contents of the thermal waters. Regarding the minor constituents,

439   Li is the least affected by secondary processes, indicating its association with the initial rock

440   dissolution process, strictly dependent on the temperature (e.g. Fouillac and Michard, 1981; Hofstra et

441   al., 2013; Cullen et al., 2021). Whereas B has a strong affinity with the vapor phase (e.g. Giggenbach,

442   1991; Arnorsson and Andresdottir, 1995; Howle et al., 2019). The high B/Cl ratios (Fig. 9) shown by

443   the thermal waters (between 0.05 and 0.08) are similar to those typically found in other liquid-

444   dominated geothermal systems (e.g. Giggenbach, 1991; Arnorsson and Andresdottir, 1995, and

445   references therein). Boron and Li^+ show a linear correlation with Cl^- (Fig. 9), suggesting that both

446   species are preferentially leached from the host rocks at high temperature (Cullen et al., 2019).

447   Furthermore, isotopic composition values of B-rich hydrothermal brines in the Puna area, falling in

448   the range of those APVC ignimbrites values (Schmitt et al., 2001; Kasemann et al., 2004), support this

449 interpretation. Additionally, some of the cold waters appear to be influenced by varying degrees of the

450 evaporation process, as mentioned earlier.

451 In addition, a recent study (Massenzio et al., 2024) has shown that boron-rich mineral precipitations

452 exist around the hot springs in the LC area. This finding suggests that the thermal waters are affected

453 by the precipitation of secondary minerals, which may incorporate or adsorb boron, thereby lowering

454 the original boron concentration (e.g., van Hinsberg et al., 2011; Reyes and Trompetter, 2012;

455 Trumbull & Slack, 2018).

456
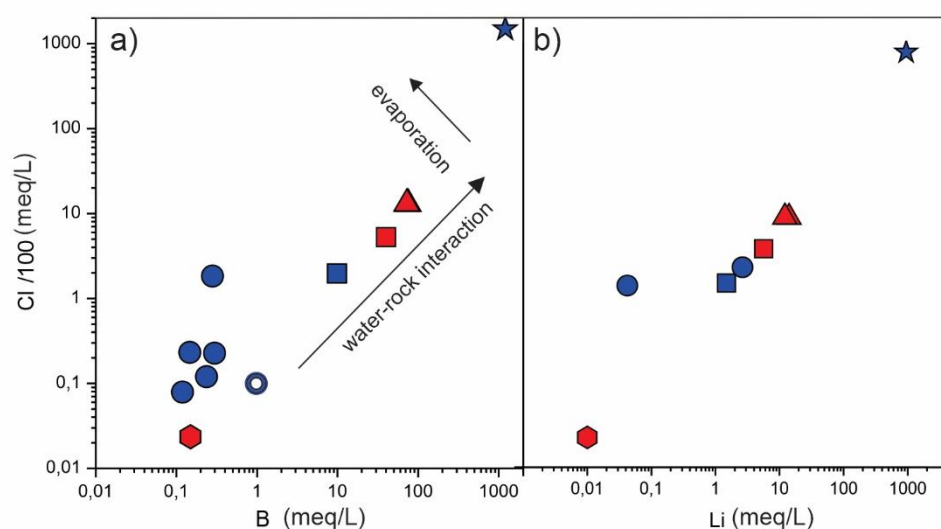
457

458 Fig. 9. (a) Cl⁻ vs. B, (b) Cl⁻ vs. Li⁺ binary diagrams for the cold and thermal waters from the CGGS. The symbols as in Fig.

459 4.

460

5.2. Origin of gases

462 The N_2-Ar-He ternary diagram (Fig. 10a), where the compositional fields of different potential

463 endmembers (crust, mantle, andesite, ASW, air; Giggenbach, 1991) are reported, shows that the N_2/Ar

464 ratios of the bubbling gases are low and consistent with those of air-saturated water (ASW: 38–42 at

465 temperature between 20 and 70 °C), ruling out the occurrence of significant N_2 contribution from an

466 extra-atmospheric source, such as microbial activity and/or thermogenic processes. Therefore, air

467 dissolved in meteoric water recharging the hydrothermal aquifer is the primary source for N_2 and Ar.

468 Reduced gas species, i.e. H_2S, CH_4, H_2 and light hydrocarbons, which occur at significant

469 concentration in the bubbling gases (Table 4), were likely generated within the hydrothermal reservoir,

470 as also suggested by the $\delta^{13}C$-CH_4 ratio measured in AC1 (Table 4). The composition of these gases

471 is likely modified secondary processes approaching the surface, where oxidizing conditions promote

472 their consumption. For example, this process is proposed to explain the SO_4^{2-}- rich composition of the

473 PBG water (Fig. 8b).

As far as the fluid source regions feeding the hydrothermal reservoir is concerned, the isotopic signatures of He and CO_2 are the most promising tools of investigation. The $^3He/^4He$ ratios (Table 4; Fig. 10b) are consistent with those measured in fluids from this region (ranging from 0.1 to 2.6 Ra; Hilton et al., 1993; Lages et al., 2021; Barry et al., 2022 and references therein). These ratios suggest a mixing between magmatic and crustal-derived fluids, resulting from intra-crustal long-term processes such as magma aging and/or fluid interaction/assimilation with ^4He-rich country rocks (Hilton et al., 1993), processes likely favored by the abnormally thick crust existing in the Puna region (55–60 km; Heit et al., 2014; Yuan et al., 2000; Lages et al., 2021).

Assuming a binary mixture between mantle (8.0 R_a; Graham, 2002; Lages et al., 2021) and crustal (0.05 R_a; Morrison and Pine, 1955) endmembers, the calculated fraction of mantle-derived helium for the maximum Rc/Ra value measured in the CGC gases (0.96; Table 4) corresponds to ~11%. In this scenario, the radiogenic helium could be added to the magmatic helium at a late stage, for example, within the hydrothermal system (Hilton et al., 1995). Alternatively, the magmatic system at CGVC could be characterized by a starting $^3He/^4He$ ratio lower than of pristine MORB, resulting from high degree of crustal assimilation. In this sense, a complex feeding system is postulated for the CGVC (Folkes et al., 2011b; Kay et al., 2011), involving a MASH (melting, assimilation, storage, and homogenization; Hildreth and Moorbath 1988) zone in the lower crust, where basaltic magmas assimilate crust and homogenize over time. It is suggested that about 50% of crustal assimilation contributes to the magma genesis of the CGVC (Kay et al., 2011; Folkes et al., 2011b), which could explain the relatively low Rc/Ra values found in the CGGS gases. This may lead to underestimations of the magmatic fluid input into the hydrothermal aquifer.

As shown in Fig. 10b, the $\delta^{13}C$-CO_2 values of the CGC gases (Table 4) are at the lower limit of the range of gases from a typical mantle source (-5 and -8 ‰ vs. V-PDB; Javoy et al., 1986). Nevertheless, the $CO_2/^3He$ ratios (up to 1.8×10^{12}; Fig. 10b), which are three orders of magnitude higher than those of gases released from the mantle ($\sim1.2 \times 10^9$; Marty and Jambon, 1987), suggest that CO_2 is mostly slab-derived, originated by degradation of organic matter and/or thermogenic processes on carbonate rocks. Following the approach of Sano and Marty (1995), which assumes that all the deviations of volcanic gases from the mantle composition are subduction/mantle derived, the contributions from the three distinct sources can be calculated as follows:

$$(\delta^{13}C\text{-}CO_2)_{meas} = M(\delta^{13}C–CO_2)_M + L(\delta^{13}C–CO_2)_L + S(\delta^{13}C–CO_2)_S \qquad (2)$$

$$1/(CO_2/^3He)_{meas} = M/(CO_2/^3He)_M + L/(CO_2/^3He)_L + S/(CO_2/^3He)_S \qquad (3)$$

$$M + L + S = 1 \qquad (4)$$

508   Assuming that each endmember component have the following values: $\delta^{13}C$-CO_2 (M = -5‰; S =
509   -30‰; L = 0‰), and $CO_2/^3He$ (M= 1.5×10^9; S = 1×10^{13}; L = 1×10^{13}).

510

511   According to Eqs. (2), (3) and (4), the contributions from the three distinct sources in the CGC gases
512   are mainly related to decarbonation reactions involving limestone (L: 69-76%), followed by significant
513   input from organic-rich sediments (S: 21-31%), with minor contribution of mantle CO_2 (M: 0.11-
514   2.44%).
515   Hydrocarbons are present at low concentrations and are primarily of thermogenic origin, as indicated
516   by the CH_4/C_2+ vs. $\delta^{13}C$–CH_4 ratio measured in the selected sample (AC1, Table 4).

517
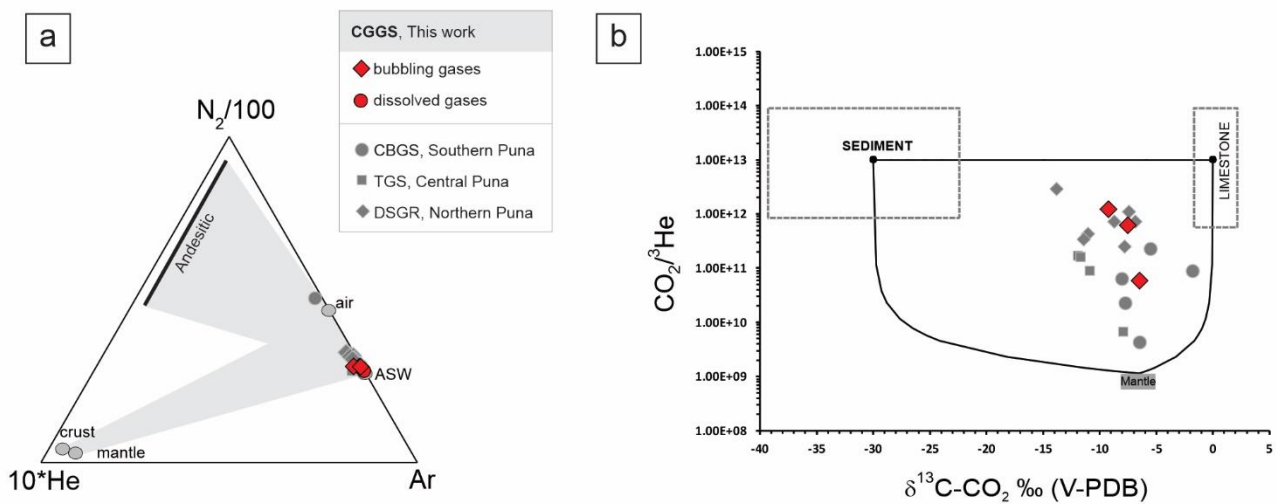
518

519   Fig. 10. (a) He–N_2-Ar ternary diagram for the gases from the CGGS. Concentrations are in mmol/mol. (b) $CO_2/^3He$ vs.
520    $\delta^{13}C$–CO_2‰ binary diagram for the gases from the CGGS. Isotopic values from other geothermal systems in the Southern,
521   Central and Northern Puna plateau are shown for comparison. CBGS: Cerro Blanco Geothermal System (Chiodi et al.,
522   2019; Barry et al., 2022). TGS: Tocomar Geothermal System (Filipovich et al., 2022; Barry et al., 2022). DSGR: Deep-
523   seated Geothermal Resource (Peralta Arnold et al., 2017). Endmember compositions for mantle, sediments and limestone
524   are also shown, along with mixing lines representing binary mixtures between the three endmember values (Sano and
525   Marty, 1995).

526

5.3. Temperature estimations of the hydrothermal reservoir

528   The degree of maturity of natural waters, i.e. the extent of water-rock interaction causing the
529   progressive modifications of the chemical feature of underground circulating fluids, can be effectively
530   evaluated based on Na-K-Mg triangular diagram (Giggenbach, 1991). In this diagram (Fig. 11a), the
531   high-chloride CGC waters plot within the field of partial equilibrium with the typical authigenic
532   mineral assemblage (which includes Na- and K-feldspars, K-micas, chlorite and silica), indicating
533   estimated temperatures in the range of ~147-187 °C. It is worth nothing that the AC1 sample exhibits

534 the lowest value, possibly due to mixing with less saline cold water, as will be discussed in section

535 5.4. The ($10K^+/[10 K^+ + Na^+]$ vs. $10Mg^{2+}/ [10Mg^{2+} + Ca^{2+}]$) geothermometer (Fig. 11b), which

536 considers the influence of Ca^{2+} in the calculations and mineral paragenesis (Chiodini et al., 1995),

537 indicates similar temperatures.

538 The concentration of SiO_2 in the liquid phase is temperature-dependent (Arnórsson, 1975), with quartz

539 dominating at higher temperatures (> 180 °C) and chalcedony becoming more significant at lower

540 temperatures (below 110 °C). In between, both polymorphs may control the solubility (Sanjuan et al.,

541 2016; Nitschke et al., 2018). The equilibrium temperatures obtained by considering quartz as the

542 primary silica mineral, ranging from 142 and 182 °C, aligns well with the temperatures estimated using

543 the Na/K geothermometer. In agreement with this, Fournier (1985) reports that in long-lived, presently

544 active systems, the solubility of quartz may control dissolved silica in reservoirs even down to 90 °C

545 (Rimstid, 1997). Considering chalcedony as the primary silica mineral, the temperatures obtained are

546 slightly lower, ranging from 115 to 162 °C, a range of values that partially overlap that of the quartz

547 geothermometer.

548
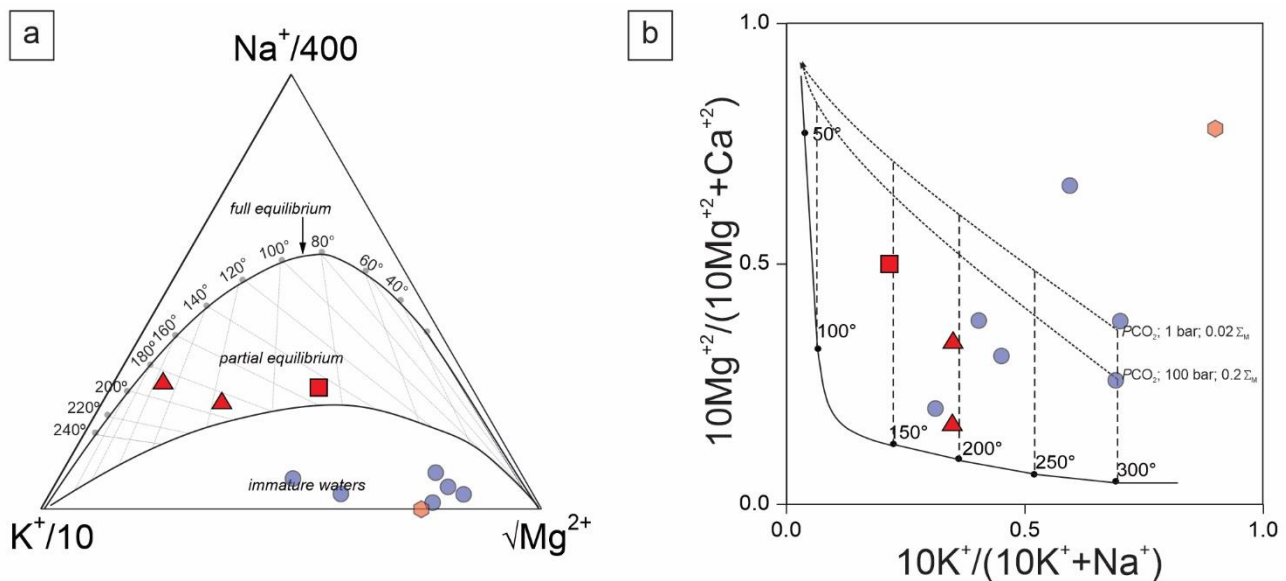
549

550 Fig. 11. (a) K^+-Na^+-Mg^{2+} ternary diagram (Giggenbach, 1988), for the studied waters from CGGS. The axes (Na/400-K/10-

551 √Mg) were modified to enlarge the low temperature area of the diagram. Partial and full equilibrium curves from 40 to 240

552 °C are reported. (b) ($10K^+/[10K^++Na^+]$ vs. $10Mg^{2+}/[10Mg^{2+}+Ca^{2+}]$) binary diagram for the studied waters from CGGS.

553 Equilibrium curves from 50 to 300 °C in presence of different mineral assemblages (Giggenbach, 1988; Chiodini et al.,

554 1995) are reported. Waters from the streams and salt lake are excluded.

555

556 Saturation index (SI = log AP/Ksp, where AP represents the ion activity product and Ksp is the

557 solubility product) for a universally valid mineral set (Ystroem et al., 2022), was calculated using the

PHREEQC v. 3.7.3 (Parkhurst and Appelo, 1999) software package, utilizing the Lawrence Livermore National Laboratory database (llnl). The calculations were performed for sample LC1, which is the closest to the full equilibrium line, from the outlet temperature 83.9 to 300 °C (using microcline to balance Al; Pang and Reed, 1998). The results indicate that minerals (except for sanidine, illite, kaollinite, and pyrophyllite) seem to achieve equilibrium (considering an uncertainty of ±0.25) in a broad range of temperatures (138-187 °C; Fig. 12a). However, it is widely recognized that achieving chemical equilibrium with a large number of minerals is unlikely in natural systems. By selecting the six best clustering minerals (quartz, albite, analcime, muscovite, diaspore, and anhydrite), the temperature is 187 °C (Fig. 12b). Such result is in good agreement with the reservoir temperatures calculated with Na/K and quartz geothermometers.
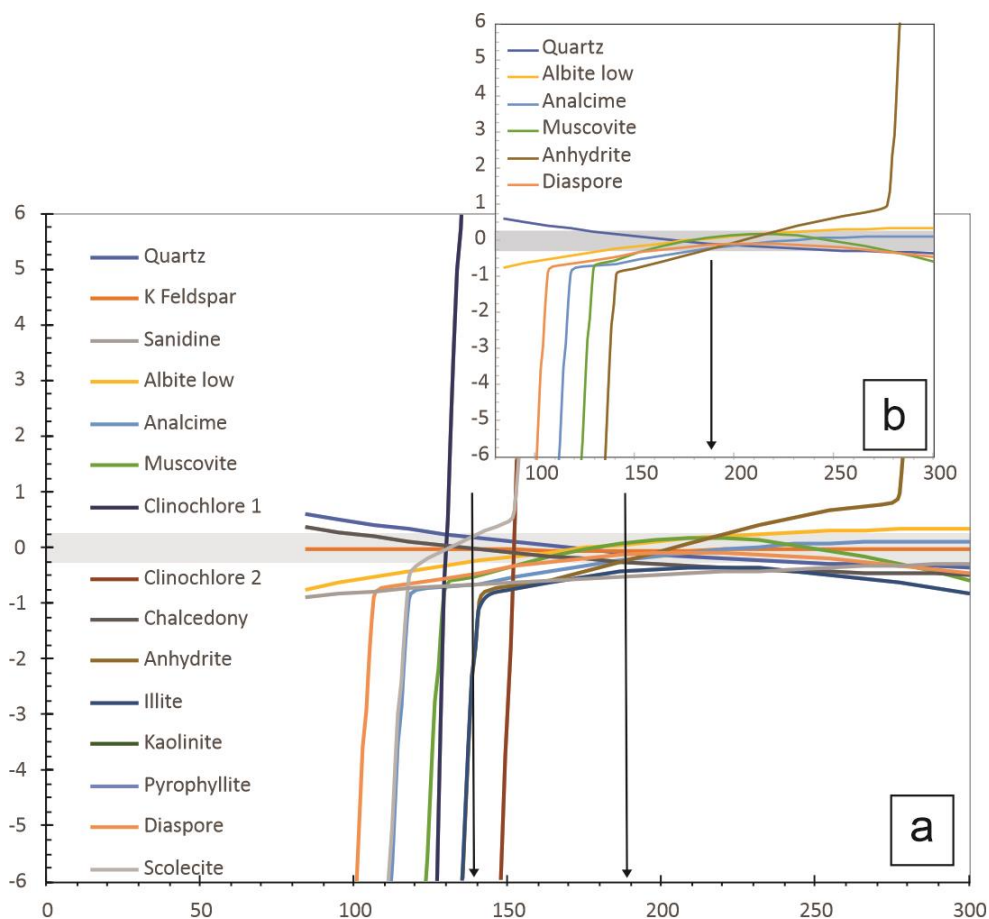
Fig. 12. (a) Temperature (°C) estimated for the LC1 sample by using the saturation indexes for various mineralogical species between the emergence temperature 83.9 to 300 °C. (b) Temperature (°C) estimated for the LC1 sample by using the saturation indexes for the six best clustering minerals between the emergence temperature 83.9 to 300 °C.

Further investigations of fluid reservoir temperatures can be achieved by analyzing gas compounds that are sensitive to variations in chemical and physical conditions. Giggenbach (1991) introduced the

576   CO_2/Ar and H_2/Ar geothermometers, depicted in Figure 13, which utilize the temperature-sensitive

577   species CO_2 and H_2 in conjunction with the chemically inert constituent Ar. This approach assumes

578   that Ar is introduced in the system by the meteoric component.

579   To avoid the effect of potential atmospheric air contamination, considering that hydrothermal fluids

580   are devoid of O_2, the Ar* values were computed, as follows:

581

582     $Ar^* = Ar - (O_2/22)$ (5)

583

584   where the $O_2/22$ ratio is the fraction of Ar from air contamination.

585   The dependence of H_2 on R_H in the two phases can be expressed as:

586

587     $Log(H_2/Ar^*)_V = R_H + 6.52 - \log(B_{Ar})$ (6)

588     $Log(H_2/Ar^*)_L = R_H + 6.52 - \log(B_{H2})$ (7)

589

590   where B_{H2} and B_{Ar} are the vapor/liquid distribution coefficient of H_2 and Ar, respectively.

591   Under the conditions controlled by the D'Amore and Panichi (1980) redox buffer (DP), the dependence

592   of CO_2/Ar^* ratios on temperature are given by:

593

594     $Log(CO_2/Ar^*)_V = Log(PCO_2) - 5.51 + 2048/T + 6.52 - Log(B_{Ar})$ (8)

595     $Log(CO_2/Ar^*)_L = Log(PCO_2) - 5.51 + 2048/T + 6.52 - Log(B_{CO2})$ (9)

596

597   where T is in K and B_{CO2} is the vapor/liquid distribution coefficient of CO_2.

598   The combination of the CO_2/Ar^* and H_2/Ar^* geothermometers from 150 to 350 °C is graphically

599   displayed in Figure 13. The CGC gases appear in disequilibrium for the redox conditions related to the

600   GT buffer typical of hydrothermal systems (Giggenbach, 1987). This indicates that the CGC gases are

601   associated with more oxidizing conditions, likely resulting from secondary processes such as H_2

602   consumption at shallow depth, Ar addition and/or CO_2 dissolution (Fig. 13), or a combination of these

603   three processes, which mask the chemical composition achieved by gases at depth, making their use

604   as geothermometers unreliable.

605
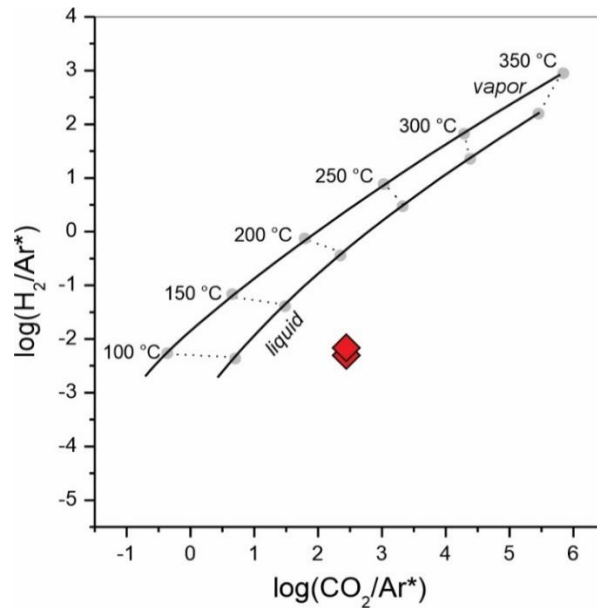
Fig. 13. Log(H_2/*Ar) vs. log(CO_2/*Ar) binary diagram for the gases from the CGGS. Solid lines refer to equilibria in the vapor and liquid phases controlled by the GT redox buffer system at temperatures from 150 to 350 °C (Giggenbach, 1987).

5.4. Geochemical conceptual model

According to the chemistry of waters and gases collected from the thermal and cold fluid manifestations, the hydrogeologic circuits in the CGC consists of: 1) surficial aquifers, directly feeding the Na^+-HCO_3^- cold springs, and 2) a relatively deep Na^+-Cl^- hydrothermal aquifer, with equilibrium temperatures reaching up to 187 °C at depth., emerges at the surface after mixing with shallow waters, facilitated by local tectonic features that promote fluid uprising (Fig. 14). Fluid circulation at shallow depth is mostly related to intense fracturing resulting from the caldera collapse, particularly noticeable in the resurgent dome and caldera borders (Fig. 5). These local lineaments (length <4,000 m; Fig. 5c) facilitate the circulation of meteoric water down to relatively shallow depth (Fig. 14), with limited water-rock interaction, which discharges along the slopes of the resurgent dome and on the caldera walls at high-altitude (>4,500 m a.s.l.). The deep hydrothermal aquifer is likely hosted within the pre-caldera basement rocks (Bm, Fig. 14), consisting of Miocene-Pliocene volcanic rocks and Proterozoic-Cambrian igneous and metamorphic rocks. The secondary permeability of these units is probably the result of the combination of the longer lineaments (length >4,000 m; Fig. 5d), likely associated with the main tectonic structures in the region with the fracturing resulting from the caldera collapse. These lineaments act as preferential paths for (i) the recharging meteoric waters also from the caldera surroundings (Fig. 14) and (ii) the deep fluid uprising to the hot springs (Fig. 14). The deposits of the Toconquis Group and Cueva Negra Ignimbrite (Tg+CN; Fig. 14), along with the basal section of the CGI, are likely responsible for confining the deep reservoir. These units probably had low primary permeability due to vapor-phase alteration and partial welding (Wright et al., 2011; Lesti et al., 2011).

630   Secondary fracturing generated in these units during the caldera collapse was likely sealed, at least

631   partially, by alteration of glass and feldspars and the subsequent generation of clays as consequence

632   of the hydrothermal fluid circulation (e.g. Henley and Ellis, 1983; Jolie et al., 2021). The occurrence

633   of a phreatic explosion crater near the LC hot springs area (Fig. 2b) testifies an over-pressurization

634   episode of the uprising hydrothermal fluids resulting from an effective sealing of the fractures at

635   relatively shallow depth. The relatively diffuse CO_2 fluxes from the soil measured in this area

636   (Massenzio et al., 2023, 2024), confirm an effective cap-rock layer.
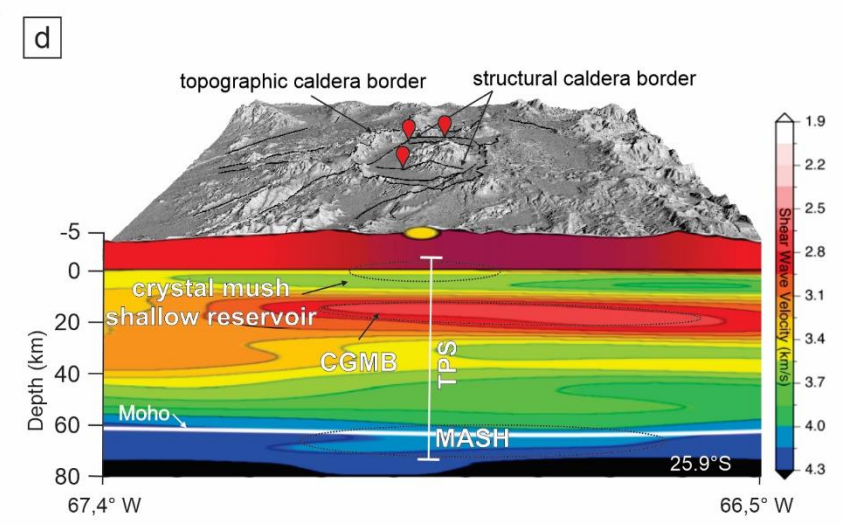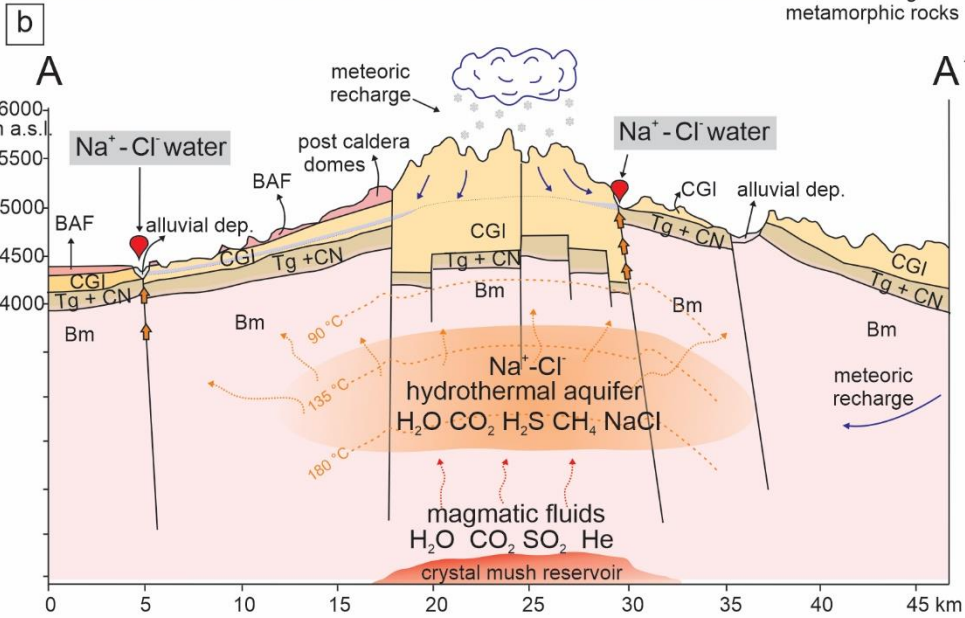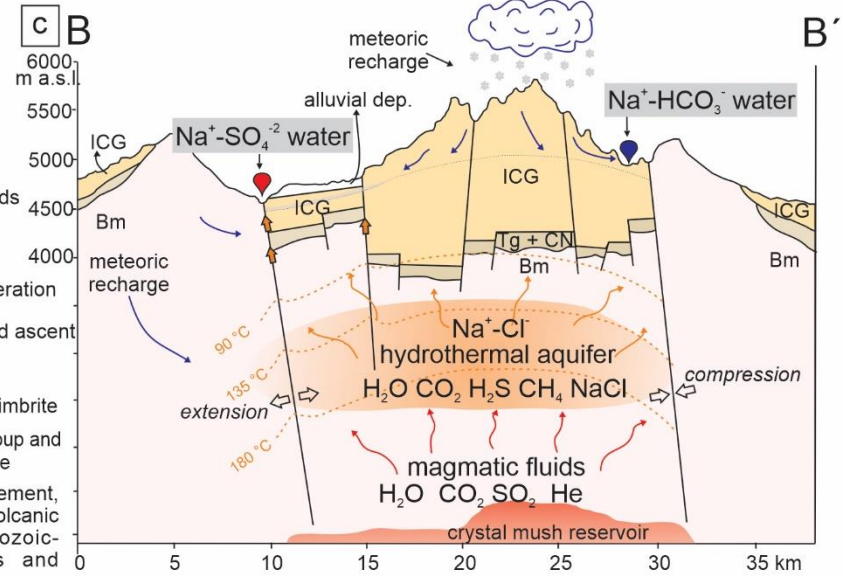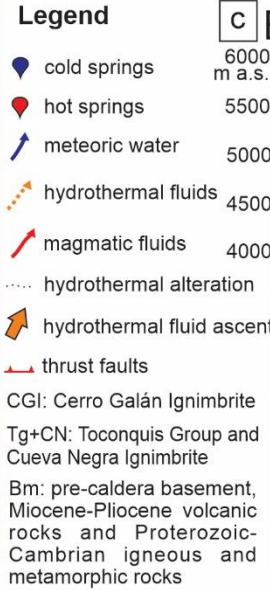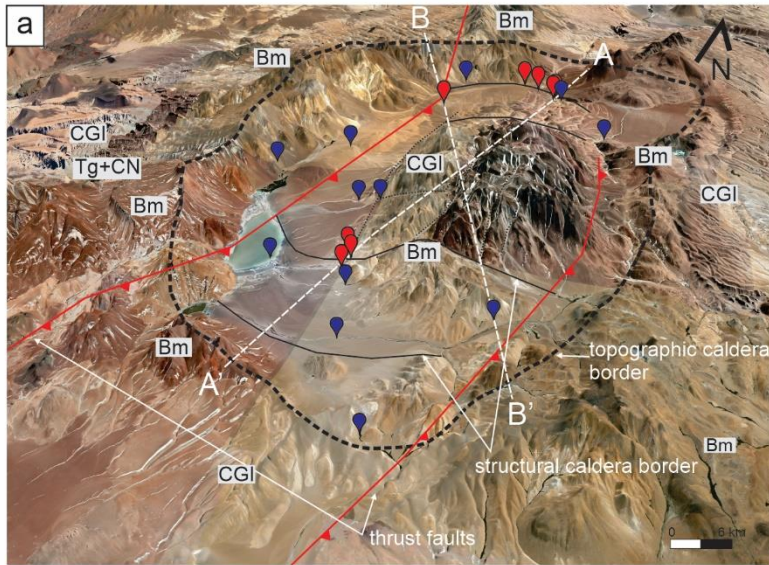
637   Considering an estimated δ^2H–H_2O vertical gradient of -2.8‰/km, based on the isotopic composition

638   of the cold springs and stream waters excluding samples clearly affected by evaporation (Table 2, Fig.

639   9), the meteoric recharge of the hydrothermal reservoir is likely located at a mean altitude of ~4,850

640   m a.s.l. As shown in Fig. 5, where the contour of 4,850 m is indicated with a purple dotted line, the

641   western sector of the CGC, where large outcrops of the pre-caldera basement exist, are probably the

642   main recharge area of the deep aquifer, whereas meteoric waters infiltrating through the top of the

643   resurgent dome recharge the shallow aquifers (red dotted line; Fig. 5). Meteoric water permeating at

644   depth reaches the reservoir formations, where they evolve due to water-rock interactions and possibly

645   receive inputs of magmatic fluids. The interaction at a local scale of hydrothermal gases, rich in H_2S

646   and meteoric water occurring at the surface produces acid-sulphate waters, such as PBG (Fig. 14), as

647   commonly occurs in calderas, where the water table is close to the ground surface due to the relatively

648   small topographic gradient (Hurwitz et al., 2003, 2007; Jolie et al., 2021).

649   The collapse of the caldera was a fault-bounded trapdoor collapse, hinged along a regional NNE-SSW

650   fault on the eastern side of the caldera (Folkes et al., 2011a). Second-order structures resulted in

651   individual blocks with differential subsidence and resurgence (piecemeal), bounded by subvertical

652   structures (Folkes et al., 2011a), that control the emplacement of post-caldera lava domes (Grocke et

653   al., 2017), and the current and fossil thermal manifestations (see section 2.2, Fig. 2). The distribution

654   of both thermal discharges and post-caldera lava domes along the western structural border of the

655   caldera is likely the result of the extension focused in this sector as a response to the resurgence

656   process, which generated compression and closure of the western structures, opposite to what occurred

657   during the caldera collapse (Folkes et al., 2011a). As seen in Figures 1 and 5, hot springs and the high

658   flow rate in the spring area (~288 m^3/h and ~765 m^3/h at LC and AC, respectively) is particularly

659   favored at the intersection between the caldera margins and the NNE-SSW oriented tectonic structures

660   (Jolie et al. 2019, 2021; Jentsch et al., 2020).

661   The lack of geophysical studies (e.g. 3D audiomagnetotellurics studies) that allow visualization of the

662   depth of the geothermal reservoir makes it difficult to estimate an accurate local geothermal gradient

663   for the CGC area. However, a preliminary estimation can be made considering the available

664   bibliographic information (Folkes et al., 2011a), which allows us to deduce average depths for the

665   contact of the Toconquis Group with the pre-caldera basement, at approximately 1,750 m below

666   ground level (Fig. 14b, c), which is considered as the top of the hydrothermal reservoir. Considering

667   an average surface water temperature of ∼10 °C (Tchilinguirian and Olivera, 2014; Salminci et al.,

668   2014), and reservoir temperatures of 182 °C and 187 °C, based on quartz and K/Na geothermometers

669   for the LC sample that be consider the best proxy of the hydrothermal fluids, respectively, the local

670   geothermal gradient for the CGC is estimated to be around 98-101 °C/km. Such an anomalous

671   geothermal gradient, greater than the average gradient of ∼60 °C/km of the southern Puna (Springer

672   and Forster, 1998; Prezzi et al., 2009; Vieira and Hamza, 2019), can be explained by the high heat flux

673   likely generated by the transcrustal plumbing system of the CGC (Fig. 14d), which includes the

674   shallow crystal mush reservoir (<4 km depth; Folkes et al., 2011b; Mulcahy et al., 2014; Grocke et al.,

675   2017), associated with the post-climactic resurgence and lava domes (Grocke et al., 2017).

676

Legend

- cold springs
- hot springs
- meteoric water
- hydrothermal fluids
- magmatic fluids
- hydrothermal alteration
- hydrothermal fluid ascent
- thrust faults

CGI: Cerro Galán Ignimbrite

Tg+CN: Toconquis Group and Cueva Negra Ignimbrite

Bm: pre-caldera basement, Miocene-Pliocene volcanic rocks and Proterozoic-Cambrian igneous and metamorphic rocks

Fig. 14. (a) *3D-Google Earth* image of the Cerro Galán caldera where the schematic cross sections A-A′ (b) and B-B'(c), are indicated. (b) Geochemical conceptual model of the Cerro Galán Geothermal System in two schematic cross sections-oriented N-S (A-A′) and NNW-SSE (B-B'), respectively. The geological cross sections from Folkes et al., 2011a. Crystal mush reservoir depth (< 4,000 m) from Grocke et al. (2017). BAF: post-caldera block and ash flow deposit. (d) 3D-Hillshade DEM illustrating the Cerro Galán caldera coupled with a west-east cross-section displaying the shear-wave velocity model from Ward et al. (2017). The transcrustal plumbing system (TPS) of the CGC, including the shallow crystal mush reservoir, the CGMB (Cerro Galán Magma Body, Ward et al. (2017) along with the lower crust MASH zone (Delph et al., 2017) is also shown.

5.5. Preliminary resource assessment

Since the 1970s, several geothermal resource assessment methods have been developed to roughly estimate the potential power capacity, ranging from the original volumetric stored heat method (Muffler and Cataldi, 1978) to more accurate and robust numerical methods using experimental design (ED) and response surface methodology (RSM) (e.g. Ciriaco et al. 2022). In geothermal greenfields or in early stages of exploration, data availability and accuracy are often limited. Therefore, it is recommended to estimate the electric potential using a probabilistic approach that incorporates Monte Carlo simulations (Ciriaco et al., 2020). The geothermal electric potential assessment for the CGGS followed the recommendations of Garg and Combs (2015) and Ciriaco et al. (2020). The input parameters involved in the volumetric stored heat equation, as well as the probability distributions assigned to reservoir parameters, are reported in Table 5.

Due to the lack of direct data or geophysical imaging, the geothermal reservoir volume was constrained based on the tectonomagmatic setting and compared with analogous resource assessments within the Southern Puna (e.g. Barcelona et al. 2022). The minimum (288.25 km^2) and maximum (475.91 km^2) areas comprise the zones bounded by the lateral N-S caldera-bounding faults and longitudinally by the inner and outer W-E caldera margin-parallel faults (Fig. 1). Notably, the minimum area spatially coincides with the highest lineament density and lineament intersection zone (Fig. 5). The reservoir thickness was estimated to range from 500 to 1,000 m using a uniform distribution, similar to the approach employed in other caldera-hosted geothermal system assessments (e.g. Barcelona et al. 2023).

While it is recommended to use triangular distributions for reservoir temperature (Garg and Combs 2015), the temperatures calculated for the CGGS consistently overlap. As a result, a minimum of 182 °C (quartz geothermometer) and a maximum of 187 °C (Na/K geothermometer) were conservatively assigned, following a uniform distribution. Regarding engineering parameters, the separator pressure was conservatively set at 9 Bar, with an abandonment temperature of 175.35 °C, to avoid significant pressure drops and scaling issues.

After 100,000 Montecarlo iterations, the forecasted electrical megawatt capacity of the reservoir indicates that the CGGS has a probable power production capacity of 2.09 MWe and 10.85 MWe at 90 and 50 % confidence levels, respectively. These are inferred resources, and further work is required to refine parameters related to reservoir geometry and recovery factor.

6. Conclusions and final remarks

Based on a comprehensive fluid geochemistry survey, a novel conceptual model of the hydrothermal system for the giant caldera Cerro Galán is presented, along with an estimation of its geothermal potential.

The presence in gas emissions from Cerro Galán area of ^{3}He/^{4}He as high as 0.96 Ra indicate that there is a variable contribution by mantle/magmatic fluids that mix with those crustal-derived characterized by ^{3}He/^{4}He of 0.01-0.05 Ra. Meteoric water circulating at depth and possibly receiving inputs of magmatic fluids, leading to the development of the hydrothermal Na-Cl aquifer, which reaches temperatures up to 187 °C at depth.

From the analysis of the lineaments, it is worth emphasizing the fundamental role played by discontinuity intersections in improving permeability within the caldera. The preliminary geothermal gradient for the CGC, estimated at around 98-101 °C/km, is likely a consequence of the high heat flux generated by the transcrustal plumbing system of the Cerro Galán caldera, including a shallow crystal mush reservoir (<4 km depth). The preliminary geothermal potential of the CGC, calculated using the volumetric method along with Monte Carlo simulations, indicates a probable power production capacity of 2.09 MWe and 10.85 MWe at 90 and 50 % confidence level, respectively.

The findings presented in this study could establish a fundamental knowledge foundation to stimulate further investigations into this giant caldera, with the focus on validating the conceptual model and progressing into more advanced stages of exploration. Detailed geophysical survey (e.g. 3D magnetotellurics) may be helpful to further confirm these evaluations.

Notably, lithium and other metal mining operations, which are operating independently from the National Interconnected System, could potentially be interested in power generation through binary cycles. By incorporating clean energy into their production processes, they would significantly reduce their carbon footprint.

7. References

Arnórsson, S. (1975). Application of the silica geothermometer in low temperature hydrothermal areas in Iceland. Am. J. Sci. (United States), 275(7). https://doi.org/10.2475/ajs.275.7.763

747   Arnorsson, S., & Andresdottir, A. (1995). Processes controlling the distribution of boron and chlorine
748   in natural waters in Iceland. Geochim. Cosmochim. Acta 59, 4125–4146.
749   https://doi.org/10.1016/0016-7037(95)00278-8

750   Báez, W., Bustos, E., Chiodi, A., García, H. P. A., Álvarez, O., Simón, V., & Folguera, A. (2023).
751   Reviewing the geodynamic impact of aseismic ridges subduction on the tectonic-magmatic
752   evolution of the Southern Puna plateau. J. South Am. Earth Sci. 104520.
753   https://doi.org/10.1016/j.jsames.2023.104520

754   Barcelona, H., Senger, M., & Yagupsky, D. (2021). Resource assessment of the Copahue geothermal
755   field. Geothermics, 90, 101987. https://doi.org/10.1016/j.geothermics.2020.101987

756   Barcelona, H., Chiodi, A., Yagupsky, D., Peri, G., Winocur, D., & Kleiman, P. (2023). Resource
757   assessment of the Cerro Blanco geothermal system. J. South Am. Earth Sci. 123, 104247.
758   https://doi.org/10.1016/j.jsames.2023.104247

759   Barry, P. H., Hilton, D. R., Fischer, T. P., De Moor, J. M., Mangasini, F., & Ramirez, C. (2013).
760   Helium and carbon isotope systematics of cold "mazuku" CO2 vents and hydrothermal gases
761   and fluids from Rungwe Volcanic Province, southern Tanzania. Chem. Geol. 339, 141-156.
762   https://doi.org/10.1016/j.chemgeo.2012.07.003

763   Barry, P. H., de Moor, J. M., Giovannelli, D., Schrenk, M., Hummer, D. R., Lopez, T., et al. (2019).
764   Forearc Carbon Sink Reduces Long-Term Volatile Recycling into the Mantle. Nature 568
765   (7753), 487–492. https://doi.org/10.1038/s41586-019-1131-5

766   Barry, P.H., De Moor, J.M., Chiodi, A., Aguilera, F., Hudak, M.R., Bekaert, D.V., Turner, S.J.,
767   Curtice, J., Seltzer, A.M., Jessen, G.L., Osses, E., Blamey, J.M., Amen´abar, M.J., Selci, M.,
768   Cascone, M., Bastianoni, A., Nakagawa, M., Filipovich, R., Bustos, E., Schrenk, M.O.,
769   Buongiorno, J., Ramírez, C.J., Rogers, T.J., Lloyd, K.G, Giovannelli, D., 2022. The helium
770   and carbon isotope characteristics of the andean convergent margin. Front. Earth Sci. 10,
771   897267. https://doi.org/10.3389/ feart.2022.897267

772   Bencini, A. (1985). Applicabilità del metodo dell'Azometina-H alla determinazione del boro nelle
773   acque naturali. Rendiconti della Societa Italiana di Mineralogia e Petrologia, 40(2), 311-316.

774   Bershaw, J., Saylor, J. E., Garzione, C. N., Leier, A., & Sundell, K. E. (2016). Stable isotope variations
775   (δ18O and δD) in modern waters across the Andean Plateau. Geochim. Cosmochim. Acta 194,
776   310-324. https://doi.org/10.1016/j.gca.2016.08.011

777   Bianchi, M., Heit, B., Jakovlev, A., Yuan, X., Kay, S.M., Sandvol, E., Alonso, R., Coira, B., Brown,
778   L., Kind, R., Comte, D. (2013). Teleseismic tomography of the southern Puna plateau in
779   Argentina and adjacent regions. Tectonophysics 586, 65–83. https://doi.
780   org/10.1016/j.tecto.2012.11.016.

781   Bona, P., Coviello, M. (2016). Valoración y gobernanza de los proyectos geotérmicos en América del
782   Sur: una propuesta metodológica. Comisión Económica para América Latina y el Caribe
783   (CEPAL).

784   Buonomano, A., Barone, G., & Forzano, C. (2023). Latest advancements and challenges of
785   technologies and methods for accelerating the sustainable energy transition. Energy Reports,
786   9, 3343-3355. https://doi.org/10.1016/j.egyr.2023.02.015

787   Calixto, F.J., Sandvol, E., Kay, S., Mulcahy, P., Heit, B., Yuan, X., Coira, B., Comte, D., Alvarado, P.
788   (2013). Velocity structure beneath the southern Puna plateau: evidence for delamination. G-
789   cubed 14 (10), 4292–4305. https://doi.org/10.1029/ 92JB00493.

790   Cas, R. A., Wright, H. M., Folkes, C. B., Lesti, C., Porreca, M., Giordano, G., & Viramonte, J. G.
791   (2011). The flow dynamics of an extremely large volume pyroclastic flow, the 2.08-Ma Cerro
792   Galán Ignimbrite, NW Argentina, and comparison with other flow types. Bull. Volcanol. 73,
793   1583-1609. https://doi.org/10.1007/s00445-011-0564-y

794   Chiodi, A. (2015). Caracterización geoquímica de Sistemas geotérmicos en dos ambientes
795   contrastados del Noroeste Argentino: Puna Austral y Sistema de Santa Bárbara. Ph.D thesis.
796   Universidad Nacional de Salta, Argentina, pp. 197.

797   Chiodi, A., Tassi, F., Báez, W., Filipovich, R., Bustos, E., Glok Galli, M., Suzaño, N., Ahumada, M.F.,
798   Viramonte, J.G., Giordano, G., Pecoraino, G., Vaselli, O. (2019). Preliminary conceptual
799   model of the Cerro Blanco caldera-hosted geothermal system (Southern Puna, Argentina):
800   Inferences from geochemical investigations. J. South Am. Earth Sci. 94,
801   102213.https://doi.org/10.1016/j.jsames.2019.102213.

802   Chiodi A., Filipovich R., Pleitavino M., Barcelona H., Esteban C. (2023). Geothermal Country update
803   of Argentina: 2020-2023. Proceedings World Geothermal Congress 2023, 15-17 September
804   15-17, Beijing, China. (p. 1).

805   Chiodi A., Filipovich, R. E., Esteban, C., Pesce, A. H., & Stefanini, V. A. (2020). Geothermal country
806   update of Argentina: 2015-2020. In Proceedings World Geothermal Congress 2020+1, April-
807   October, Iceland. (p. 1).

808   Chiodini, G., 1996. Gases dissolved in groundwaters: analytical methods and examples of applications
809   in central Italy. In: Marini, L., Ottonello, G. (Eds.), Rome Seminar on Environmental
810   Geochemistry. Pacini Editore, Castelnuovo d Porto, Rome (Italy), pp.135–148.

811   Chiodini, G., Frondini, F., & Marini, L. (1995). Theoretical geothermometers and PCO2 indicators for
812   aqueous solutions coming from hydrothermal systems of medium-low temperature hosted in
813   carbonate-evaporite rocks. Application to the thermal springs of the Etruscan Swell, Italy. J.
814   App. Geochem. 10(3), 337-346. https://doi.org/10.1016/0883-2927(95)00006-6

815   Ciriaco, A. E., Zarrouk, S. J., & Zakeri, G. (2020). Geothermal resource and reserve assessment
816   methodology: Overview, analysis and future directions. Renewable Sustainable Energy Rev.
817   119, 109515. https://doi.org/10.1016/j.rser.2019.109515

818   Ciriaco, A. E., Uribe, M. H., Zarrouk, S. J., Downward, T., Omagbon, J. B., Austria, J. J. C., &
819   Yglopaz, D. M. (2022). Probabilistic geothermal resource assessment using experimental
820   design and response surface methodology: The Leyte geothermal production
821   field. Geothermics, 103, 102426.

822   Colmenar-Santos, A., Palomo-Torrejón, E., Rosales-Asensio, E., & Borge-Diez, D. (2018). Measures
823   to remove geothermal energy barriers in the European Union. Energies, 11(11), 3202.
824   https://doi.org/10.3390/en11113202

825   Contino F., Moret S., Limpens G., Jeanmart H. (2020). Whole-energy system models: The advisors
826   for the energy transition, Progress in Energy and Combustion Science, Volume 81, 100872.
827   https://doi.org/10.1016/j.pecs.2020.100872.

828   Cullen, J. T., Hurwitz, S., Barnes, J. D., Lassiter, J. C., Penniston-Dorland, S., Kasemann, S. A., &
829   Thordsen, J. J. (2019). Temperature-dependent variations in mineralogy, major element
830   chemistry and the stable isotopes of boron, lithium and chlorine resulting from hydration of
831   rhyolite: Constraints from hydrothermal experiments at 150 to 350°C and 25 MPa. Geochim.
832   Cosmochim. Acta 261, 269–287. https://doi.org/10.1016/j.gca.2019.07.012

833   Craig, H., Gordon, L. I., & Horibe, Y. (1963). Isotopic exchange effects in the evaporation of water:
834   1. Low-temperature experimental results. J. Geophys. Res. 68(17), 5079-5087.
835   https://doi.org/10.1029/JZ068i017p05079

836   DeCelles, P.G., Zandt, G., Beck, S.L., Currie, C.A., Ducea, M.N., Kapp, P., Gehrels, G.E., Carrapa,
837   B., Quade, J., Schoenbohm, L.M., (2015) Cyclical orogenic processes in the Cenozoic central
838   Andes, in DeCelles, P.G., Ducea, M.N., Carrapa, B., and Kapp, P.A., eds., Geodynamics of a
839   Cordilleran Orogenic System: The Central Andes of Argentina and Northern Chile: Geological
840   Society of America Memoir 212, p. 459-490. https://doi.org/10.1130/2015.1212(22)

841   Delph, J. R., Ward, K. M., Zandt, G., Ducea, M. N., & Beck, S. L. (2017). Imaging a magma plumbing
842   system from MASH zone to magma reservoir. EPSL 457, 313-
843   324.https://doi.org/10.1016/j.epsl.2016.10.008.

844   D'Amore, F., & Panichi, C. (1980). Evaluation of deep temperatures of hydrothermal systems by a
845   new gas geothermometer. Geochim. Cosmochim. Acta, 44(3), 549-556.
846   https://doi.org/10.1016/0016-7037(80)90051-4

847

848 de Silva, S. L., & Gregg, P. M. (2014). Thermomechanical feedbacks in magmatic systems:
849   Implications for growth, longevity, and evolution of large caldera-forming magma reservoirs
850   and their supereruptions. J. Volcanol. Geotherm. Res. 282, 77-91.
851   https://doi.org/10.1016/j.jvolgeores.2014.06.001

852 de Silva, S. L., & Kay, S. M. (2018). Turning up the heat: high-flux magmatism in the Central Andes.
853   Elements: An International Magazine of Mineralogy, Geochemistry, and Petrology, 14(4), 245-
854   250. https://doi.org/10.2138/gselements.14.4.245.

855 Farnfield, H. R., Marcilla, A. L., & Ward, N. I. (2012). Arsenic speciation and trace element analysis
856   of the volcanic río Agrio and the geothermal waters of Copahue, Argentina. Sci. Total Environ.
857   433, 371-378. https://doi.org/10.1016/j.scitotenv.2012.05.098

858 Filipovich R., Chiodi A., Báez W., Ahumada F., Invernizzi C., Taviani S., Aldega L., Tassi F., Barrios
859   A., Corrado S., Groppelli G., Norini G., Bigi S., Caricchi C., De Benedetti A., De Astis G.,
860   Becchio R., Viramonte J.G., Giordano G. (2022). Structural analysis and fluid geochemistry as
861   tools to assess the potential of the Tocomar geothermal system, Central Puna (Argentina).
862   Geothermics, 98, 10227. https://doi.org/10.1016/j.geothermics.2021.102297

863 Fiorella, R. P., Poulsen, C. J., Zolá, R. S. P., Jeffery, M. L., & Ehlers, T. A. (2015). Modern and long-
864   term evaporation of central Andes surface waters suggests paleo archives underestimate
865   Neogene elevations. EPSL, 432, 59-72. https://doi.org/10.1016/j.epsl.2015.09.045

866 Folkes, C.B., de Silva, S.L., Wright, H.M., & Cas, R.A.F. (2011a). Geochemical homogeneity of a
867   long-lived, large silicic system; evidence from the Cerro Galán caldera, NW Argentina. Bull.
868   Volcanol. 73, 1455-1486. https://doi.org/10.1007/s00445-011-0511-y.

869 Folkes, C., Wright, H., Cas, R., de Silva, S., Lesti, C., & Viramonte, J.G. (2011b). A re-appraisal of
870   the stratigraphy and volcanology of the Cerro Galán volcanic system, NW Argentina. Bull.
871   Volcanol. 73, 1427-1454. https://doi.org/10.1007/s00445-011-0459-y

872 Folkes, C. B., de Silva, S. L., Schmitt, A. K., & Cas, R. A. (2011c). A reconnaissance of U-Pb zircon
873   ages in the Cerro Galán system, NW Argentina: Prolonged magma residence, crystal recycling,
874   and crustal assimilation. J. Volcanol. Geotherm. Res. 206(3-4), 136-147.
875   https://doi.org/10.1016/j.jvolgeores.2011.06.001

876 Fouillac, C., & Michard, G. (1981). Sodium/lithium ratio in water applied to geothermometry of
877   geothermal reservoirs. Geothermics 10(1), 55-70. https://doi.org/10.1016/0375-
878   6505(81)90025-0

879 Fournier, R. O. (1985). The behavior of silica in hydrothermal solutions.

Francis, P. W., & Baker, M. C. W. (1978). Sources of two large ignimbrites in the central Andes: some Landsat evidence. J. Volcanol. Geotherm. Res. 4(1-2), 81-87. https://doi.org/10.1016/0377-0273(78)90029-X

Francis, P. W., O'Callaghan, L., Kretzschmar, G. A., Thorpe, R. S., Sparks, R. S. J., Page, R. N., ... & Gonzalez, O. E. (1983). The Cerro Galan ignimbrite. Nature 301(5895), 51-53. https://doi.org/10.1038/301051a0

Freymuth, H., Brandmeier, M., & Wörner, G. (2015). The origin and crust/mantle mass balance of Central Andean ignimbrite magmatism constrained by oxygen and strontium isotopes and erupted volumes. Contrib. Mineral. 169, 1-24.https://doi.org/10.1007/s00410-015-1152-5.

Friedman, J. D., & Heiken, G. (1977). Volcanoes and volcanic landforms. Skylab Explores the Earth. NASA Spec. Pap, 380, 137-170.

Garg, S. K., & Combs, J. (2015). A reformulation of USGS volumetric "heat in place" resource estimation method. Geothermics 55, 150-158. https://doi.org/10.1016/j.geothermics.2015.02.004

Gielen, D., Boshell, F., Saygin, D., Bazilian, M. D., Wagner, N., & Gorini, R. (2019). The role of renewable energy in the global energy transformation. Energy strategy rev. 24, 38-50. https://doi.org/10.1016/j.esr.2019.01.006

Giggenbach, W. F. (1978). The isotopic composition of waters from the El Tatio geothermal field, Northern Chile. Geochim. Cosmochim. Acta 42(7), 979-988. https://doi.org/10.1016/0016-7037(78)90287-9

Giggenbach, W. F. (1987). Redox processes governing the chemistry of fumarolic gas discharges from White Island, New Zealand. J. Appl. Geochem. 2(2), 143-161. https://doi.org/10.1016/0883-2927(87)90030-8

Giggenbach, W. F. (1988). Geothermal solute equilibria. derivation of Na-K-Mg-Ca geoindicators. Geochim. Cosmochim. Acta 52(12), 2749-2765. https://doi.org/10.1016/0016-7037(88)90143-3

Giggenbach, W. F. (1991). Chemical techniques in geothermal exploration. Application of geochemistry in geothermal reservoir development, 119-144.

Giggenbach, W.F. (1997). The origin and evolution of fluids in magmatic-hydrothermal systems. In: Barnes, H.L. (Ed.), Geochemistry of Hydrothermal Ore Deposits. John Wiley and Sons, New York, pp. 737–789.

Giggenbach, W.F., & Goguel, R. (1989). Collection and Analysis of Geothermal and Volcanic Water and Gas Discharges, Unpublished Report. Chemistry Division. Department of Scientific and Industrial Research, Petone, New Zealand, pp. 81.

914   Giordano, G., & Caricchi, L. (2022). Determining the state of activity of transcrustal magmatic systems
915   and their volcanoes. Annu. Rev. Earth Planet. Sci. 50, 231-259.
916   https://doi.org/10.1146/annurev-earth-032320-084733

917   Giordano, G., Pinton, A., Cianfarra, P., Baez, W., Chiodi, A., Viramonte, J., Norini, G., Groppelli, G.
918   (2013). Structural control on geotermal circulation in the Cerro Tuzgle–Tocomar geothermal
919   volcanic area (Puna plateau, Argentina). J. Volcanol. Geotherm. Res. 249, 77-94.
920   https://doi.org/10.1016/j.jvolgeores.2012.09.009

921   Giordano, G., De Benedetti, A. A., Bonamico, A., Ramazzotti, P., & Mattei, M. (2014). Incorporating
922   surface indicators of reservoir permeability into reservoir volume calculations: Application to
923   the Colli Albani caldera and the Central Italy Geothermal Province. Earth Sci. Rev. 128, 75-
924   92. https://doi.org/10.1016/j.earscirev.2013.10.010

925   Goff, F., & Janik, C. J. (2000). Geothermal systems. Encyclopedia of volcanoes, 2000, 817-834.

926   Gonfiantini, R., Roche, M. A., Olivry, J. C., Fontes, J. C., & Zuppi, G. M. (2001). The altitude effect
927   on the isotopic composition of tropical rains. Chem. Geol. 181(1-4), 147-167.
928   https://doi.org/10.1016/S0009-2541(01)00279-0

929   Graham, D. W. (2002). Noble gas isotope geochemistry of mid-ocean ridge and ocean island basalts:
930   Characterization of mantle source reservoirs. Rev. Mineral. Geochem. 47(1), 247-317.

931   Grocke, S. B., Andrews, B. J., & de Silva, S. L. (2017). Experimental and petrological constraints on
932   long-term magma dynamics and post-climactic eruptions at the Cerro Galán caldera system,
933   NW   Argentina.   J.   Volcanol.   Geotherm.   Res.   347,   296-311.
934   https://doi.org/10.1016/j.jvolgeores.2017.09.021

935   Heit, B., Bianchi, M., Yuan, X., Kay, S.M., Sandvol, E., Kumar, P., Kind, R., Alonso, R.N., Brown,
936   L.D., Comte, D. (2014). Structure of the crust and the lithosphere beneath the southern Puna
937   plateau   from   teleseismic   receiver   functions.   EPSL   385,   1-11.
938   https://doi.org/10.1016/j.epsl.2013.10.017.

939   Henley, R. W., & Ellis, A. J. (1983). Geothermal systems ancient and modern: a geochemical review.
940   Earth Sci. Rev. 19(1), 1-50. https://doi.org/10.1016/0012-8252(83)90075-2

941   Hofstra, A. H., Todorov, T. I., Mercer, C. N., Adams, D. T., & Marsh, E. E. (2013). Silicate melt
942   inclusion evidence for extreme pre-eruptive enrichment and post-eruptive depletion of lithium
943   in silicic volcanic rocks of the western United States: Implications for the origin of lithium-
944   rich brines. Econ Geol. 108, 1691–1701. https://doi.org/10.2113/econgeo.108.7.1691

945   Hildreth, W., & Moorbath, S. (1988). Crustal contributions to arc magmatism in the Andes of Central
946   Chile. Contrib. Mineral. 98, 455-489. https://doi.org/10.1007/BF00372365

Hilton, D. R., Hammerschmidt, K., Teufel, S., & Friedrichsen, H. (1993). Helium isotope characteristics of Andean geothermal fluids and lavas. EPSL 120(3-4), 265-282. https://doi.org/10.1016/0012-821X(93)90244-4

Hilton, D. R. (1996). The helium and carbon isotope systematics of a continental geothermal system: results from monitoring studies at Long Valley caldera (California, USA). Chemical Geology 127(4), 269-295.

Hoefs, J. (2008). Stable Isotope Chemistry. Springer, Berlin, New York, pp. 260.

Howle, J. F., Evans, W. C., Galloway, D. L., Hsieh, P. A., Hurwitz, S., Smith, G. A., & Nawikas, J. (2019). Hydraulic, Geochemical, and Thermal Monitoring of an Aquifer System in the Vicinity of Mammoth Lakes, Mono County, California. U.S. Geological Survey Open-File Report, No. 2019-1063. USGS. Retrieved from https://doi.org/10.3133/ofr20191063

Hongn, F.D., Seggiaro, R.E., Monardi, C.R., Alonso, R.N., Gonzalez, R.E., Igarzabal, A.P., & Moya, F. (2001). Hoja Geológica 2566-III Cachi: Programa Nacional de Cartas Geológicas de la República Argentina, Servicio Geológico Minero Argentino. scale 1:250,000. Instituto de Geología y Recursos Minerales. Boletín Nro 548.

Inguaggiato, S., & Rizzo, A. (2004). Dissolved helium isotope ratios in ground-waters: a new technique based on gas–water re-equilibration and its application to Stromboli volcanic system. J. Appl. Geochem. 19(5), 665-673. https://doi.org/10.1016/j.apgeochem.2003.10.009.

Japanese International Cooperation Agency (JICA), 1992. The feasibility study on the Northem Neuqu´en Geothermal Development Project Ente Provincial de Energía de la Provincia del Neuquén, 1992. JICA-EPEN, Neuquén, p. 89 (unpublished).

Javoy, M., Pineau, F., & Delorme, H. (1986). Carbon and nitrogen isotopes in the mantle. Chem. Geol. 57(1-2), 41-62. https://doi.org/10.1016/0009-2541(86)90093-8

Jentsch, A., Jolie, E., Jones, D. G., Taylor-Curran, H., Peiffer, L., Zimmer, M., & Lister, B. (2020). Magmatic volatiles to assess permeable volcano-tectonic structures in the Los Humeros geothermal field, Mexico. J. Volcanol. Geotherm. Res. 394, 106820. https://doi.org/10.1016/j.jvolgeores.2020.106820.

Jolie, E., Hutchison, W., Driba, D. L., Jentsch, A., & Gizaw, B. (2019). Pinpointing deep geothermal upflow in zones of complex tectono-Volcanic degassing: New insights from Aluto volcano, Main Ethiopian Rift. Geochem. Geophys. 20(8), 4146-4161. https://doi.org/10.1029/2019GC008309

Jolie, E., Scott, S., Faulds, J., Chambefort, I., Axelsson, G., Gutiérrez-Negrín, L. C., Regenspurg, S., Ziegler, M., Ayling, B., Richter, A. & Zemedkun, M. T. (2021). Geological controls on

980　　　　geothermal resources for power generation. Nat. Rev. Earth Environ. 2(5), 324-339.
981　　　　https://doi.org/10.1038/s43017-021-00154-y

982　Jones, B. E., & Grant, W. D. (1999). Microbial diversity and ecology of the Soda Lakes of East Africa.
983　　　　In Microbial Biosystems: New Frontiers: Proceedings of the 8th International Symposium for
984　　　　Microbial Ecology (2000). Atlantic Canada Society for Microbial Ecology, Halifax, Canada
985　　　　(pp. 681-687).

986　Kaiser, J. F., de Silva, S., Schmitt, A. K., Economos, R., & Sunagua, M. (2017). Million-year melt–
987　　　　presence in monotonous intermediate magma for a volcanic–plutonic assemblage in the Central
988　　　　Andes: contrasting histories of crystal-rich and crystal-poor super-sized silicic magmas. EPSL
989　　　　457, 73-86. https://doi.org/10.1016/j.epsl.2016.09.048

990　Kasemann, S. A., Meixner, A., Erzinger, J., Viramonte, J. G., Alonso, R. N., & Franz, G. (2004). Boron
991　　　　isotope composition of geothermal fluids and borate minerals from salar deposits (central
992　　　　Andes/NW Argentina). J. South Am. Earth Sci. 16(8), 685-697.

993　Karolytė, R., Johnson, G., Györe, D., Serno, S., Flude, S., Stuart, F. M., Chivas, A., Boyce, A., &
994　　　　Gilfillan, S. M. (2019). Tracing the migration of mantle CO_2 in gas fields and mineral water
995　　　　springs in south-east Australia using noble gas and stable isotopes. Geochim. Cosmochim. Acta
996　　　　259, 109-128. https://doi.org/10.1016/j.gca.2019.06.002

997　Kay, S. M., & Coira, B. L. (2009) Shallowing and steepening subduction zones, continental
998　　　　lithospheric loss, magmatism, and crustalflow under the Central Andean Altiplano- Puna
999　　　　Plateau. In: Kay, S.M., Ramos, V.A., Dickinson, W.R. (Eds.), Backbone of the Americas:
1000　　　　Shallow Subduction, Plateau Uplift, and Ridge and Terrane Collision. Geol. Soc. Mem., 204–
1001　　　　229. https://doi.org/10.1130/2009.1204(11)

1002　Kay, S. M., Coira, B., Wörner, G., Kay, R. W., & Singer, B. S. (2011). Geochemical, isotopic and
1003　　　　single crystal 40 Ar/39 Ar age constraints on the evolution of the Cerro Galán ignimbrites.
1004　　　　Bull. Volcan. 73, 1487-1511. https://doi.org/10.1007/s00445-010-0410-7

1005　Krieger, M., Kurek, K. A., & Brommer, M. (2022). Global geothermal industry data collection: A
1006　　　　systematic　　　　review.　　　　Geothermics　　　　104,　　　　102457.
1007　　　　https://doi.org/10.1016/j.geothermics.2022.102457.

1008　Kulp, T. R., Han, S., Saltikov, C. W., Lanoil, B. D., Zargar, K., & Oremland, R. S. (2008). Effects of
1009　　　　Imposed Salinity Gradients on Dissimilatory Arsenate Reduction, Sulfate Reduction, and Other
1010　　　　Microbial Processes in Sediments from Two California Soda Lakes. AEM 73(16), 5130-5137.
1011　　　　https://doi.org/10.1128/AEM.00771-07

1012　Hurwitz, S., Kipp, K. L., Ingebritsen, S. E., & Reid, M. E. (2003). Groundwater flow, heat transport,
1013　　　　and water table position within volcanic edifices: Implications for volcanic processes in the

Cascade Range. J. Geophys. Res. Solid Earth 108(B12), 2557. https://doi.org/10.1029/2003JB002565.

Hurwitz, S., Christiansen, L. B., & Hsieh, P. A. (2007). Hydrothermal fluid flow and deformation in large calderas: Inferences from numerical simulations. J. Geophys. Res. Solid Earth 112(B2). https://doi.org/10.1029/2006JB004689

Lages, J., Rizzo, A. L., Aiuppa, A., Robidoux, P., Aguilar, R., Apaza, F. (2021). Crustal Controls on Light Noble Gas Isotope Variability along the Andean Volcanic Arc. Geochem. Perspect. Lett. 19, 45–49. doi:10.7185/geochemlet.2134

Lesti, C., Porreca, M., Giordano, G., Mattei, M., Cas, R. A., Wright, H. M., Folkes, C. Viramonte, J.G. (2011). High-temperature emplacement of the Cerro Galán and Toconquis Group ignimbrites (Puna Plateau, NW Argentina) determined by TRM analyses. Bull. Volcanol. 73, 1535-1565. https://doi.org/10.1007/s00445-011-0536-2

Li, K., Bian, H., Liu, C., Zhang, D., & Yang, Y. (2015). Comparison of geothermal with solar and wind power generation systems. Renewable Sustainable Energy Rev. 42, 1464-1474. https://doi.org/10.1016/j.rser.2014.10.049

Liang, X., Sandvol, E., Kay, S., Heit, B., Yuan, X., Mulcahy, P., Chen, C., Brown, L., Comte, D., Alvarado, P. (2014). Delamination of southern Puna lithosphere revealed by body wave attenuation tomography. J. Geophys. Res. Solid Earth 119(1), 549-566. https://doi.org/10.1002/2013JB010309.

Lipman, P. W., & Bachmann, O. (2015). Ignimbrites to batholiths: Integrating perspectives from geological, geophysical, and geochronological data. Geosphere 11(3), 705-743. https://doi.org/10.1130/GES01091.1

López, D.L., Bundschuh, J., Birkle, P., Armienta, M.A., Cumbal, L., Sracek, O., Cornejo, L., & Ormachea, M., (2012). Arsenic in volcanic geothermal fluids of Latin America. Sci. Total Environ. 429, 57–75. https://doi.org/10.1016/j. scitotenv.2011.08.043.

Ma, Y., Zhang, W., Xue, Y., Zhou, P., Ventosa, A., & Grant, W. D. (2004). Bacterial diversity of the Inner Mongolian Baer Soda Lake as revealed by 16S rRNA gene sequence analyses. Extremophiles 8, 45-51. https://doi.org/10.1007/s00792-003-0358-z

Mamyrin, B.A., Tolstikhin, I.N. (1984). Helium Isotopes in Nature. Elsevier, Amsterdam.

Marty, B., & Jambon, A. (1987). C3He in volatile fluxes from the solid Earth: implications for carbon geodynamics. EPSL 83(1-4), 16-26. https://doi.org/10.1016/0012-821X(87)90047-1

Mason, E., Edmonds, M., & Turchyn, A. V. (2017). Remobilization of crustal carbon may dominate volcanic arc emissions. Science 357(6348), 290-294. https://doi.org/10.1126/science.aan5049

Massenzio, A., Chiodi, A., Lamberti, C., Murray, J., Filipovich, R., Salduondo, J., Nuñez, N., Gómez, M., Agusto, M., Viramonte, J. (2023). Estudio geoquímico y geológico en superficie del sistema geotermal Cerro Galán: desgasificación de CO2, temperatura del suelo y alteración hidrotermal. Proceedings 18° Encuentro del Centro Internacional de Ciencias de la Tierra (E-ICES 18), Argentina.

Massenzio, A., Chiodi, A., Lamberti, C., Murray, J., Filipovich, R., Salduondo, J., Agusto, M., Viramonte, J. (2024). Desgasificación difusa de dióxido de carbono y mineralización secunedaria en los suelos del sistema geotermal Cerro Galán (Catamarca, Puna Austral). Revista de la Asociación Geológica Argentina 81(2).

Moeck, I. S. (2014). Catalog of geothermal play types based on geologic controls. Renewable Sustainable Energy Rev. 37, 867-882. https://doi.org/10.1016/j. rser.2014.05.032.

Morrison, P., & Pine, J. (1955). Radiogenic Origin of the Helium Isotopes in Rock. Ann. N. Y. Acad. Sci. 62 (3), 71–92. doi:10.1111/j.1749-6632.1955.tb35366.x

Muffler, P., & Cataldi, R. (1978). Methods for regional assessment of geothermal resources. Geothermics 7(2-4), 53-89. https://doi.org/10.1016/0375-6505(78)90002-0

Mulcahy, P., Chen, C., Kay, S.M., Brown, L.D., Isacks, B.L., Sandvol, E., Heit, B., Yuan, X., Coira, B.L. (2014). Central Andean mantle and crustal seismicity beneath the Southern Puna plateau and the northern margin of the Chilean-Pampean flat slab. Tectonics 33(8), 1636-1658. https://doi.org/10.1002/2013TC003393.

Murray, J., Guzmán, S., Tapia, J., & Nordstrom, D. K. (2023). Silicic volcanic rocks, a main regional source of geogenic arsenic in waters: Insights from the Altiplano-Puna plateau, Central Andes. Chemi. Geol. 629, 121473. https://doi.org/10.1016/j.chemgeo.2023.121473

Newell, D. L., Jessup, M. J., Hilton, D. R., Shaw, C. A., & Hughes, C. A. (2015). Mantle-derived helium in hot springs of the Cordillera Blanca, Peru: Implications for mantle-to-crust fluid transfer in a flat-slab subduction setting. Chemical Geology 417, 200-209. https://doi.org/10.1016/j.chemgeo.2015.10.003

Nicholson, K. (1993). Geothermal fluids: chemistry and exploration techniques. Springer-Verlag, 268 p, Berlin.

Nitschke, F., Held, S., Neumann, T., & Kohl, T. (2018). Geochemical characterization of the Villarrica geothermal system, Southern Chile, part II: site-specific re-evaluation of SiO2 and Na-K solute geothermometers. Geothermics 74, 217-225. https://doi.org/10.1016/j.geothermics.2018.03.006

Ozima, M., & Podosek, F.A. (1983). Noble Gas Geochemistry. Cambridge University Press, Cambridge, p. 367.

Palomo, E., Colmenar-Santos, A., & Rosales-Asensio, E. (2022). Measures to Remove Geothermal Energy Barriers in the European Union. In Potential of Low-Medium Enthalpy Geothermal Energy: Hybridization and Application in Industry (pp. 9-45). Cham: Springer International Publishing. https://doi.org/10.1007/978-3-030-95626-4_2

Pan, S. Y., Gao, M., Shah, K. J., Zheng, J., Pei, S. L., & Chiang, P. C. (2019). Establishment of enhanced geothermal energy utilization plans: Barriers and strategies. Renewable energy 132, 19-32. https://doi.org/10.1016/j.renene.2018.07.126

Pang, Z. H., & Reed, M. (1998). Theoretical chemical thermometry on geothermal waters: problems and methods. Geochim. Cosmochim. Acta 62(6), 1083-1091. https://doi.org/10.1016/S0016-7037(98)00037-4

Parkhurst, D. L., & Appelo, C. A. J. (1999). User's guide to PHREEQC (Version 2): A computer program for speciation, batch-reaction, one-dimensional transport, and inverse geochemical calculations. Water-resources investigations report, 99(4259), 312.

Pecoraino, G., D'Alessandro, W., & Inguaggiato, S. (2015).The other side of the coin: geochemistry of alkaline lakes in volcanic areas. In: Volcanic lakes, 219-237. Advances in volcanology. Springer-Verlag, Berlin, Heidelberg. https://doi.org/10.1007/978-3-642-36833-2_9

Peralta Arnold, Y. P., Cabassi, J., Tassi, F., Caffe, P. J., & Vaselli, O. (2017). Fluid geochemistry of a deep-seated geothermal resource in the Puna plateau (Jujuy Province, Argentina). J. Volcanol. Geotherm. Res. 338, 121-134. https://doi.org/10.1016/j.jvolgeores.2017.03.030

Pfenninger, S., Hawkes, A., & Keirstead, J. (2014). Energy systems modeling for twenty-first century energy challenges. Renewable Sustainable Energy Rev. 33, 74-86. https://doi.org/10.1016/j.rser.2014.02.003.

Poreda, R., & Craig, H. (1989). Helium isotope ratios in circum-Pacific volcanic arcs. Nature 338(6215), 473-478. https://doi.org/10.1038/338473a0

Prezzi, C.B., Gotze, H.J., Schmidt, S., (2009). 3D density model of the Central Andes. Phys. Earth Planet. Inter. 177 (3–4), 217–234.

Ray, M. C., Hilton, D. R., Muñoz, J., Fischer, T. P., & Shaw, A. M. (2009). The effects of volatile recycling, degassing and crustal contamination on the helium and carbon geochemistry of hydrothermal fluids from the Southern Volcanic Zone of Chile. Chem.l Geol. 266(1-2), 38-49. https://doi.org/10.1016/j.chemgeo. 2008.12.026

Reyes, A. G., & Trompetter, W. J. (2012). Hydrothermal water-rock interaction and the redistribution of Li, B and Cl in the Taupo Volcanic Zone, New Zealand. Chem. Geol. 314–317, 96–112. https://doi.org/10.1016/j.chemgeo.2012.05.002

1114 Rimstidt, J. D. (1997). Quartz solubility at low temperatures. Geochim. Cosmochim. Acta 61(13),
1115   2553-2558. https://doi.org/10.1016/S0016-7037(97)00103-8

1116 Rizzo, A. L., Barberi, F., Carapezza, M., Di. Piazza, A., Francalanci, L., Sortino, F., & D'Alessandro,
1117   W. (2015), New mafic magma refilling a quiescent volcano: Evidence from He-Ne-Ar isotopes
1118   during the 2011–2012 unrest at Santorini, Greece, Geochem. Geophys. Geosyst., 16, 798–814,
1119   doi:10.1002/2014GC005653

1120 Rizzo, A., Caracausi, A., Chavagnac, V., Nomikou, P., Polymenakou, P., Mandalakis, M., Kotoulas,
1121   A., Castillo, A., Lampridou, D. (2016). Kolumbo submarine volcano (Greece): An active
1122   window into the Aegean subduction system. Scientific Reports 6 28013 (2016).
1123   https://doi.org/10.1038/srep28013

1124 Rollinson, H. (1993). Using Geochemical Data. Longman, London, UK, pp. 352.

1125 Salminci, P. M., Tchilinguirian, P., & Lane, K. J. (2014). Bordos and boundaries: Sustainable
1126   agriculture in the high altitude deserts of Northwest Argentina, AD 850-1532.

1127 Sanci, R., Panarello, H. O., & Gozalvez, M. R. (2020). Environmental isotopes as tracers of mining
1128   activities and natural processes: A case study of San Antonio de los Cobres River Basin, Puna
1129   Argentina. J. Geochem. Explor. 213, 106517. https://doi.org/10.1016/j.gexplo.2020.106517

1130 Sancho-Tomás, M., Somogyi, A., Medjoubi, K., Bergamaschi, A., Visscher, P.T., Van Driessche,
1131   A.E., Gérard, E., Farias, M.E., Contreras, M. and Philippot, P., (2020). Geochemical evidence
1132   for arsenic cycling in living microbialites of a High Altitude Andean Lake (Laguna Diamante,
1133   Argentina). Chem. Geol. 549, 119681. https://doi.org/10.1016/j.chemgeo.2020.119681

1134 Sanjuan, B., Millot, R., Innocent, C., Dezayes, C., Scheiber, J., & Brach, M. (2016). Major
1135   geochemical characteristics of geothermal brines from the Upper Rhine Graben granitic
1136   basement with constraints on temperature and circulation. Chem. Geol. 428, 27-47.
1137   https://doi.org/10.1016/j.chemgeo.2016.02.021

1138 Sano, Y., & Marty, B., 1995. Origin of carbon in fumarolic gas from island arcs. Chem. Geol. 119,
1139   265-274.

1140 Schmitt, A. K., Kasemann, S., Meixner, A., & Rhede, D. (2002). Boron in central Andean ignimbrites:
1141   implications for crustal boron cycles in an active continental margin. Chem. Geol. 183(1-4),
1142   333-347.

1143 Sparks, R. S. J., Francis, P. W., Hamer, R. D., Pankhurst, R. J., O'callaghan, L. O., Thorpe, R. S., &
1144   Page, R. (1985). Ignimbrites of the cerro Galan caldera, NW Argentina. J. Volcanol. Geotherm.
1145   Res. 24(3-4), 205-248. https://doi.org/10.1016/0377-0273(85)90071-X

1146 Stepanenko, T., Soria, M. N., Saona Acuña, L. A., Lencina, A. I., & Farías, M. E. (2020). A unique
1147   natural laboratory to study polyextremophile microorganisms: Diamante Lake as a window to

the origin of life. Microbial Ecosystems in Central Andes Extreme Environments: Biofilms, Microbial Mats, Microbialites and Endoevaporites, 113-120. https://doi.org/10.1007/978-3-030-36192-1_8

Springer, M., & Forster, A., (1998). Heat-flow density across the Central Andean subduction zone. Tectonophysics 291 (1–4), 123–139.

Stimac, J., Goff, F., & Goff, C. J. (2015). Intrusion-Related geotermal systems. In: Sigurdsson, H. (Ed.), Encyclopedia of Volcanoes. Academic Press., pp. 799–822.

Sun, Y., Gao, P., & Razzaq, A. (2023). How does fiscal decentralization lead to renewable energy transition and a sustainable environment? Evidence from highly decentralized economies. Renewable Energy 206, 1064-1074. https://doi.org/10.1016/j.renene.2023.02.069

Tapia, J., Murray, J., Ormachea, M., Tirado, N., & Nordstrom, D. K. (2019). Origin, distribution, and geochemistry of arsenic in the Altiplano-Puna plateau of Argentina, Bolivia, Chile, and Perú. Sci. Total Environ. 678, 309-325. https://doi.org/10.1016/j.scitotenv.2019.04.084

Tassi, F., Vaselli, O., Capaccioni, B., Giolito, C., Duarte, E., Fernandez, E., Minissale, A., & Magro, G. (2005). The hydrothermal-volcanic system of Rincon de la Vieja volcano (Costa Rica): A combined (inorganic and organic) geochemical approach to understanding the origin of the fluid discharges and its possible application to volcanic surveillance. J. Volcanol. Geotherm. Res. 148(3-4), 315-333.

Tchilinguirian, P., & Olivera, D. E. (2014). Late Quaternary paleoenvironments, South Andean Puna (25º-27ºS), Argentina. In Hunter-gatherers from a high-elevation desert: People of the Salt Puna (northwest Argentina). Oxford, UK: Archaeopress, 43-69.

Truesdell, A. H., & Hulston, J. R. (1980). Isotopic evidence on environments of geothermal systems. Handbook of environmental isotope geochemistry. Vol. 1.

Trumbull, R. B., & Slack, J. F. (2018). Boron isotopes in the continental crust: Granites, pegmatites, felsic volcanic rocks, and related ore deposits. In H. Marschall & G. Foster (Eds.), Boron isotopes. Advances in Isotope Geochemistry (pp. 249–272). Springer. Retrieved from https://doi.org/10.1007/978-3-319-64666-4_10

van Hinsberg, V. J., Henry, D. J., & Marschall, H. R. (2011). Tourmaline: An ideal indicator of its host environment. The Canadian Mineralogist 49, 1–16. https://doi.org/10.3749/canmin.49.1.1

Vaselli, O., Tassi, F., Montegrossi, G., Capaccioni, B., Giannini, L. (2006). Sampling and analysis of volcanic gases. Acta Volcanologica 18, 65–76.

Vieira, F., & Hamza, V., (2019). Assessment of geothermal resources of South America-a new look. IJTHFA 2 (1), 46–57.

Ward, K. M., Delph, J. R., Zandt, G., Beck, S. L., & Ducea, M. N. (2017). Magmatic evolution of a Cordilleran flare-up and its role in the creation of silicic crust. Sci. Rep. 7(1), 9047.https://doi.org/10.1038/s41598-017-09015-5.

Webster, J. G., & Nordstrom, D. K. (2003). Geothermal arsenic: The source, transport and fate of arsenic in geothermal systems. In Arsenic in ground water: geochemistry and occurrence Boston, MA: Springer US, pp. 101-125.

Wise, D. U., Funiciello, R., Parotto, M., & Salvini, F. (1985). Topographic lineament swarms: Clues to their origin from domain analysis of Italy. Geol. Soc. Am. Bull. 96(7), 952–967.

Witter, J. B., Trainor-Guitton, W. J., & Siler, D. L. (2019). Uncertainty and risk evaluation during the exploration stage of geothermal development: A review. Geothermics 78, 233-242. https://doi.org/10.1016/j.geothermics.2018.12.011

Whitfield, M. (1978). Activity coefficients in natural waters. In: Pytkowicz, R.M. (Ed.), Activity Coefficients in Electrolyte Solutions. CRC Press, Boca Raton, Florida, pp.153–300.

Wright, H. M., Folkes, C. B., Cas, R. A., & Cashman, K. V. (2011). Heterogeneous pumice populations in the 2.08-Ma Cerro Galán Ignimbrite: implications for magma recharge and ascent preceding a large-volume silicic eruption. Bull. Volcanol. 73, 1513-1533.https://doi.org/10.1007/s00445-011-0525-5.

Ystroem, L. H., Nitschke, F., & Kohl, T. (2022). MulT_predict-An optimised comprehensive multicomponent geothermometer. Geothermics 105, 102548. https://doi.org/10.1016/j.geothermics.2022.102548

Yuan, X., Sobolev, S.V., Kind, R., Oncken, O., Bock, G., Asch, G., Schurr, B., Graeber, F., Rudloff, A., Hanka, W., Wylegalla, K., Tibi, R., Haberland, C., Rietbrock, A., Giese, P., Wigger, P., Rower, P., Zandt, G., Beck, S., Wallace, T., Pardo, M., Comte, D. (2000). Subduction and collision processes in the Central Andes constrained by converted seismic phases. Nature 408, 958–961. https://doi.org/ 10.1038/35050073.

Acknowledgements

1217

1218

1219

1220

1221

1222

1223

1224

1225

1226

1227

1228

1229

1230

1231

Table captions

Site	ID	Type	Latitude	Longitude	Altitude	T	pH	ORP	EC	Total Alkalinity	FR
Aguas Calientes hot springs area	AC0	stream	-25.829333	-66.917861	4507	7.2	5.66		2140	253	
	AC1	hot spring	-25.825587	-66.922427	4471	61.1	6.36	127.1	6546	195	~459
	AC2	hot spring	-25.828715	-66.923101	4493	24.9	7.11		6480	285	
	AC3	hot spring	-25.810046	-66.947507	4402	30.2	6.64		8490	75	~306
	AC4	hot spring	-25.812742	-66.937091	4429	21.3	6.85		2890		
Piscinas Burbujeantes del Galán area	PBG	bubbling pool	-25.858167	-66.992861	4624	80	4.95	-6.1	568	10	
La Colcha hot springs area	LC1	hot spring	-26.033084	-66.986289	4706	83.9	6.78	48.3	10580	300	~288
	LC2	hot spring	-26.026559	-66.990803	4102	36.8	6.08		10490	290	
	LC3	hot spring	-26.039974	-66.988490	4667	69.4	6.36	1.9	9816	288	
Cerro Galán caldera area	RLM	stream	-26.080869	-66.925438	4710	1.0	6.84		130	59	
	CGVF1	cold spring	-26.132199	-66.941689	4637	19.7	6.51		300	55	
	CGVF2	cold spring	-26.060640	-66.905864	4777	13.3	6.83		260	21	
	CGVF3	cold spring	-26.051265	-66.981625	4699	18.2	6.49		480	90	
	CGVF4	cold spring	-25.989254	-66.987177	4919	18.3	6.46		660	33	
	CGVF5	hot spring	-25.987837	-67.000473	4788	21.9	7.03		2780	234	
	CGVF6	cold spring	-25.929589	-67.029793	4701	3.72	6.70	33.3	2413	105	
	CGVF7	cold spring	-25.956227	-67.064948	4664	14	6.60		280	40	
	CGVF8	cold spring	-25.820146	-66.988017	4557	4.94	6.09	266.8	1386	33	
	CGVF9	cold spring	-25.887059	-66.880850	4710	17.6	6.65		160	39	
	LD	lake	-26.044047	-67.031996	4589	6.78	9.20	159.8	217000	9870	

Table 1: Sampling sites. Geographic coordinates, altitude (m a.s.l.), T: outlet temperature (°C), pH values, ORP (mV), EC: electrical conductivity (µS/cm), Total Alkalinity (mg/L $CaCO_3$), and FR: Flow rate (m^3/h) of the studied waters.

ID	CO_3^{-2}	HCO_3^-	F^-	Cl^-	Br^-	NO_3^-	SO_4^{2-}	HS^-	Ca^{2+}	Mg^{2+}	Na^+	K^+	NH_4^+	Li^+	B	SiO_2	STD	$\delta^{18}O$	δ^2H	CI %
AC0		308	0.33	198	0.32	1.7	26.1	n.a.	50.3	10.5	143	15.4	0.05	1.5	9.8	n.a.	765	-7.7	-51	-5.85
AC1		238	2.7	528	0.75	6.8	56.4	12.3	24.7	2.5	421	11.6	0.05	5.7	40	108	1460	-6.9	-52	-0.45
AC3																		-7.01	-52	
PBG		13	0.17	2.4	1.4	2.3	78.8	17	2.0	0.7	2.90	2.6	24.1	0.01	0.16	71	218	-1.6	-55	-7.9
LC1	0.1	366	4.5	1300	1.6	1.5	88.6	12	38.1	0.8	994	53.1	1.5	14.1	75.1	152	3100	-5.8	-52	2.01
LC2																		-6.11	-54	
LC3	0.1	351	4.7	1306	10.8	n.a.	67.1	n.a.	89.5	4.5	853	45.8	n.a.	12.1	72.5	207	3025	n.a.	n.a.	-1.44
RLM	0.6	71	n.a.	10	n.a.	n.a.	9.4	n.a.	11.7	1.7	14.4	4.2	n.a.	n.a.	1.0	104	230	-5.78	-45	-5.98
CGVF1	0.6	66	n.a.	12	n.a.	n.a.	7.6	n.a.	11.5	0.4	18.5	4.2	n.a.	n.a.	0.2	n.a.	120	-2.70	-31	-1.94
CGVF2																		-6.57	-47	
CGVF3	0.9	108	n.a.	22.7	n.a.	n.a.	13.5	n.a.	19.3	0.5	33.9	1.5	n.a.	n.a.	0.3	n.a.	200	-5.50	-40	-3.32
CGVF4		40	n.a.	23.2	n.a.	n.a.	33.5	n.a.	16.1	1.00	29.6	2.0	n.a.	n.a.	0.1	n.a.	150	-8.90	-53	5.05
CGVF5																		-6.78	-51	
CGVF6		128	0.55	311.1	1.2	1.97	12.2	n.a.	30.1	5.9	163.5	24.0	n.a.	2.6	n.a.	n.a.	681	-5.71	-48	-7.11
CGVF7		49	n.a.	7.9	n.a.	n.a.	10.3	n.a.	9.8	0.4	13.1	1.1	n.a.	n.a.	0.1	n.a.	90	-7.93	-52	-4.75
CGVF8		40	0.18	183.2	1.1	34.1	18.4	n.a.	88.4	5.5	26.6	6.2	n.a.	0.04	0.3	30	434	-7.83	-51	-4.71
CGVF9																		-6.23	-40	
LD	542.5	10941	161.09	148492	855.9	n.a.	10371	n.a.	334.8	290.4	90926	5239	n.a.	947	1204	n.a.	270305	n.a.	n.a.	-5.42
GCN																		-7.69	-38	

Table 2: Chemical and stable isotopic ($\delta^{18}O$-H_2O and δD-H_2O in ‰ vs. V-SMOW) composition of the studied waters. Concentrations are in mg/L. IC: ionic charge imbalance. n.a. not analyzed.

ID	Mn	Fe	Se	Ba	Al	Co	Ni	Cu	Zn	Sb	AsT	As (III)	As (V)
AC1	75	27.0	3.4	10.0	7.8	<2.4	<5	3.4	5.8	<10	5370	1750	770
AC3	<0.1	<2	<1	6.4	<2.5	<2.4	<5	<0.2	<0.5	n.a.	n.a.	n.a.	n.a.
PBG	24	80	<1	9.3	9.5	<2.4	<5	2.3	11.0	<10	140	4	<0.5
LC1	162	15.0	<1	14.0	12.0	<2.4	<5	7.5	5.9	199.0	7920	3070	2710
LC2	198	5.34	6.5	12.4	<2.5	<2.4	<5	<0.2	<0.5	n.a.	n.a.	n.a.	n.a.
LC3	119	20.0	2.9	12.0	12.0	<2.4	<5	8.4	15.0	98.0	11300	2530	3260
RLM	6.4	72	<1	2.1	17.0	<2.4	<5	3.7	6.0	<10	48	<0.5	5
CGVF8	8.5	7.0	<1	35.0	2.6	<2.4	<5	<2	7.4	<10	n.a.	n.a.	n.a.
LD	0.46	2.9	<1	12.0	<1.1	<2.4	<5	306	<2	<10	342330	280	276740

Table 3: Chemical composition (in µg/L) of minor elements of the studied waters. AsT: total Arsenic. n.a.: not analyzed.

ID	Latitude	Longitude	Type	CO_2	H_2S	N_2	CH_4	Ar	O_2	Ne	H_2	He	CO
AC1	-25.825587	-66.922427	dissolved	157	n.d.	669	0.005	16	158	0.0083	n.d.	0.0018	n.d.
AC1	-25.825587	-66.922427	bubbling	851	1.1	139	0.16	3.31	5.61	0.0018	0.018	0.0036	n.d.
PBG	-25.858167	-66.992861	bubbling	879	n.d.	115	0.009	2.75	3.16	0.0015	n.d.	0.0015	n.d.
LC1	-26.033084	-66.986289	dissolved	300	n.d.	549	0.005	14	137	0.0075	n.d.	0.0021	n.d.
LC1	-26.033084	-66.986289	bubbling	851	1.3	141	0.22	3.27	3.44	0.0018	0.015	0.0105	n.d.

ID	C_2H_6	C_3H_8	$i\text{-}C_4H_{10}$	$n\text{-}C_4H_{10}$	$i\text{-}C_4H_8$	$i\text{-}C_5H_{12}$	$n\text{-}C_5H_{12}$	C_6H_6	$\delta^{13}C\text{-}CO_2$	Rc/Ra	$^4He/^{20}Ne$	$\delta^{13}C\text{-}CH_4$
AC1	n.d.	n.d.	n.d.	n.d.	n.d.	n.d.	n.d.	n.d.			0.22	
AC1	0.0025	0.00015	0.00019	0.00014	0.00025	0.00009	0.00008	0.0013	-7.51	0.27	2.00	-31.8
PBG	n.d.	n.d.	n.d.	n.d.	n.d.	n.d.	n.d.	n.d.	-9.25	0.34	1.00	
LC1	n.d.	n.d.	n.d.	n.d.	n.d.	n.d.	n.d.	n.d.			0.28	
LC1	0.0031	0.00021	0.00026	0.00022	0.00036	0.00013	0.00012	0.0015	-6.51	0.96	5.83	

Table 4: Chemical and stable isotope ($\delta^{13}C\text{-}CO_2$, and $\delta^{13}C\text{-}CH_4$ (both expressed as ‰ vs. V-PDB), and R/Ra composition of the studied gases. $^4He/^{20}Ne$ ratio is also reported. Concentrations are in mmol/mol. n.d: not detected.

| Input parameter | Unit | Value | | Distribution |
		min.	max.	
Area	km^2	288.25	475.91	uniform
Thickness	m	500	1000	uniform
Reservoir temperature	°C	182	187	uniform
Volumetric heat capacity	kJ/m^3.K^{-1}	2650		
Recovery factor	%	0	20	uniform
Separator temperature (9 bar)	°C	175.35		
Condenser temperature	°C	40		
Conversion efficiency	%	0.08	0.09	uniform
Specific heat of vaporization (9 bar)	kJ/kg	2030.4		
Plan capacity factor	%	80.1	95	uniform
Power plant life	years	30		

Table 5: List of parameters used for the resource assessment.